A Flexible Underwater Pressure Sensor Array for Artificial Lateral Line Applications

by

Frank M. Yaul

B.S., Massachusetts Institute of Technology (2011)

Submitted to the Department of Electrical Engineering and Computer Science, Massachusetts Institute of Technology in partial fulfillment of the requirements for the degree of

Master of Engineering in Electrical Engineering

at the

MASSACHUSETTS INSTITUTE OF TECHNOLOGY

September 2011

Author .....
Department of Electrical Engineering and Computer Science
August 19th, 2011

Certified by .....
Jeffrey H. Lang
Professor of Electrical Engineering and Computer Science
Thesis Supervisor

Accepted by .....
Dennis M. Freeman
Chairman, Master of Engineering Thesis Committee
Department of Electrical Engineering and Computer Science

A Flexible Underwater Pressure Sensor Array for Artificial Lateral Line Applications

by

Frank M. Yaul

Submitted to the Department of Electrical Engineering and Computer Science,
Massachusetts Institute of Technology
on August 19th, 2011, in partial fulfillment of the
requirements for the degree of
Master of Engineering in Electrical Engineering

Abstract

This thesis develops a flexible elastomer-based underwater pressure sensor array. When mounted onto the hull of an aquatic vehicle, the array enables obstacle detection, identification and tracking, and can help the vehicle reduce its hydrodynamic drag by providing information about the surrounding flow. This thesis begins with the development of a carbon black-PDMS elastomer material set. Using the material set, a 4-point-probe resistive strain gauge is developed and combined with a pressure-concentrating PDMS diaphragm to create the MEMS-based pressure sensors. A one-dimensional array of 4 sensors is fabricated, and the dynamic response of the sensors is characterized and modelled. Based on the model, the operating conditions required for a linear sensor response are determined. This thesis ends with proof-of-concept underwater object and wave detection experiments demonstrating that the sensor can function as an artificial lateral line.

The sensors exhibit a $1.38 \cdot 10^{-3}$ fractional resistance change per 100 pascals, which yields a maximum pressure resolution of 1.5 pascals for a power consumption of 10 μW per sensor, ignoring the power dissipated by the amplification circuitry and parasitic resistances. Each sensor is capable of transducing up to a 1 kPa pressure differential across its diaphragm, though the sensor may respond to signals of this amplitude at arbitrary underwater depth due to the use of a pressure equilibration scheme. The overall array has a 15 mm spatial resolution. An upper bound for the bandwidth of the diaphragms is calculated to be 940 Hz, ignoring viscous damping due to air, water, and the PDMS. Additionally, sensor operation while mounted to a hull with a 0.5 m radius of curvature is demonstrated.

Thesis Supervisor: Jeffrey H. Lang
Title: Professor of Electrical Engineering and Computer Science

Acknowledgments

Forever am I grateful for my family, my friends, and my colleagues; all of you have made this work possible. To honor your support, I have tried my best to invest myself honestly in this work. The MIT Sea Grant program also deserves my gratitude for funding my tenure as a research assistant under Project R/RT-2/RCM-17, letting me, for the most part, concentrate on doing solid science and engineering. Though I am not experienced, I gather it is not often that one is granted the opportunity to single-mindedly try to understand something better, shielded from the demands of a deliverable.

The Squitch Team deserves much gratitude for the weekly discussions providing help with fabrication and materials synthesis and characterization. I'd like to thank Sarah Paydavosi for, among other things, sharing with me her experiences with "independent" research. I also thank Professor Vladimir Bulović for effectively being my second advisor. I want to thank him for his insight and ideas, and for helping provide me with the steadfastness and persistence to understand and use elastomer materials which, at the start of the project, defied repeatability. Additionally, credit is due to the National Science Foundation Center for Energy Efficient Electronics (E3S) for supporting this team's research on nanocomposite materials.

Michael Triantafyllou's group has also played a huge role, being the people who will hopefully come to use the sensor developed in this thesis. I want to especially thank Vicente Fernandez for assisting with the water tank experiments, for giving great suggestions and guidance, and for generally being interested in seeing the sensor work. I would also like to thank Professor Triantafyllou for his support, patience, and earnest interest in seeing the sensor project succeed. I hope his research goals of biomimetic sensing and propulsion in AUVs are realized. The Singapore MIT Alliance for Research and Technology (SMART) deserves recognition for being a major supporter of this group.

Kevin Lee, a student in Rajeev Ram's group, deserves ample thanks for putting up with my mess-making abilities and for helping me get the project off of the ground. Kevin, thank you for your kindness, especially since you did not have any stake in my work. Samuel Chang and Dave Otten, though not directly involved in this thesis project, worked with me on my first research project and have continued to help me.

Professor Jeffrey Lang has been a mentor and advisor to me during my undergraduate years and my Master's thesis. I cannot thank him enough. He has given me an extraordinary amount of independence in my work and allowed me to truly steer my project, while still being eager to help through observing individual experiments or even by trudging through calculations with me. He readily provides insightful comments and clever ideas. He has helped me understand what research is about, how to do good science, and how the scientific community operates. Professor Lang, thank you.

Along the course of this past year, there were so many times when I became lost or stuck. Oliver and Steve, thank you so much for moving me along with bikes, games, and your simple and strong passion for life. Thank you Robert and Huayu, for being an incredibly enthusiastic about so many things, from cooking to exploring. Thank you Gabe, for reminding me about some very important things in our lives. Thank you Aseema - I'm glad I was able to talk with you about "how" research "is" - you are very perceptive. Thilani, thank you - you're always in my classes and you have a great positive attitude - thank you for putting up with me. I'm happy you love

circuits. Andrew, thanks for speaking with me about art. We're so different, but thank you for your trust. Monica and Eugenia, thank you for your companionship - I have enjoyed all the adventures.

Mom, thank you for carrying me all this time. Without your support and love, there is no way I would have made it here. Dad, you were the one who got me interested in science. Thanks for showing me your thesis; I never imagined I'd be writing one of these. Finally, I want to thank God for the grace, guidance, and spirit which has allowed me to reach this point. I will try my best in the future. Thank you Lord for everything.

Everyone, it has been fun. This section of my thesis is the one I have enjoyed writing the most. I hope you enjoy the rest.

Contents

Chapter 1

Introduction

1.1 Motivation: The Lateral Line Application

The objective of this thesis is to create a flexible underwater pressure sensor array capable of transducing pressure signals on the order of 10 pascals. The array comprises individual pressure sensing cells arranged in a one-dimensional strip, which is designed to be externally mounted along the curved hull of an aquatic vehicle as shown in Figure 1-1. The relative motion between objects and the water surrounding the vehicle generates pressure signals which may be detected by the array. Thus, the array enables a detailed evaluation of local fluid mechanics around an aquatic vehicle. This information can be used to enhance the vehicle's propulsive efficiency and maneuverability [24], and to passively detect underwater obstacles or targets [7].

The array is intended to mimic a fish's lateral line, which is diagrammed in Figure 1-2. The lateral line is a flow-sensing organ that all fish possess. It consists of a canal lined with an array of drag-based flow sensors called neuromasts. Pressure gradients between adjacent pores on the canal induce flow through the canal which is picked up by the neuromasts [10]. This flow-sensing array gives the fish knowledge of pressure distributions in the water [3].

Many complex behaviors of fish may be attributed to this sensory organ. For example, the Blind Mexican Cavefish *(Astyanax fasciatus)*, uses its lateral line to navigate in cluttered environments in the absence of light [16, 26]. Other behaviors

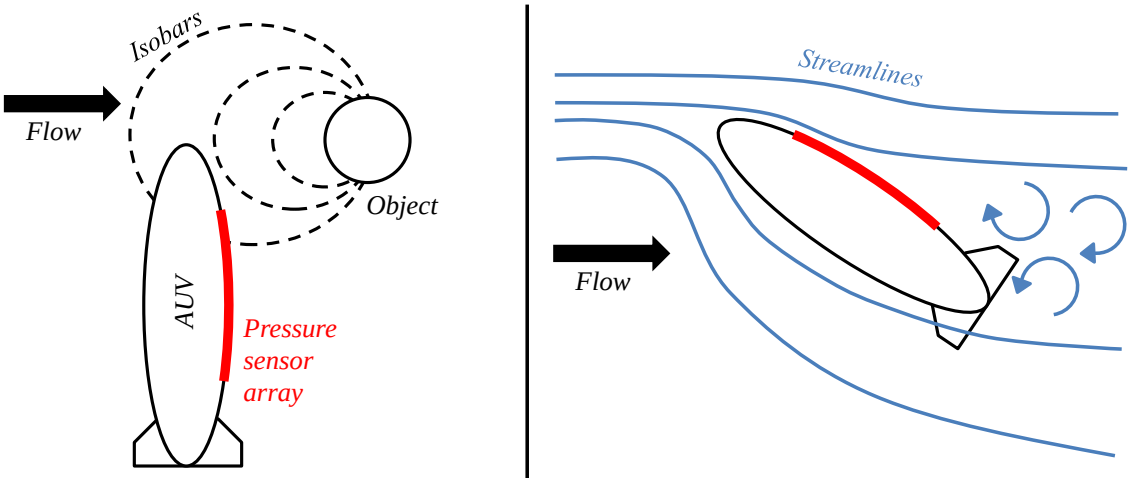

(a) Object detection and identification

(b) Detection of flow seperation

Figure 1-1: Flexible underwater pressure sensor array applications.

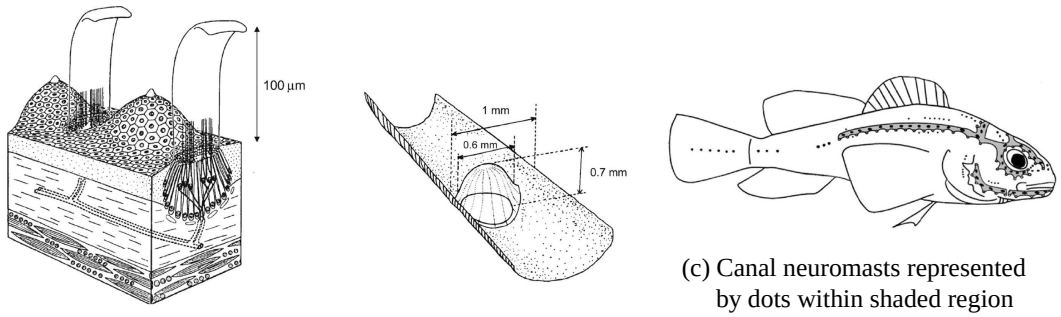

(a) Neuromast diagram

(b) Neuromast inside a canal

(c) Canal neuromasts represented by dots within shaded region on the fish body diagram.

Figure 1-2: Diagram of a fish's lateral line organ, courtesy of [29].

of fish such as tracking prey by their wake [18], and discriminating the size, velocity, and shape of nearby objects [25] can also be attributed to the lateral line. Giving such functionality to underwater vehicles is a current topic of research [29, 28], and is the motivation for this thesis.

Current technologies for remote detection of underwater objects include sonar and vision-based systems [31]. However, sonar suffers from multipath propogation issues in the cluttered seabed environment, and vision-based systems are limited by the turbidity of the sea water. Additionally, both systems are forms of active sensing and must emit energy in the form of acoustic waves or light in order to operate. Thus, they are inherently less energy-efficient and less covert when compared to passive detection systems such as the pressure sensor array described in this thesis.

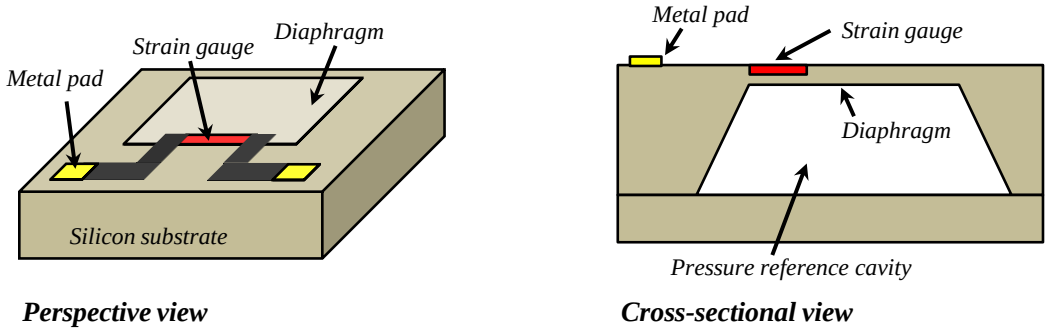

Figure 1-3: Diagram of a typical silicon MEMS pressure sensor.

Autonomous Underwater Vehicles (AUVs) in particular have a very limited energy supply and often operate in cluttered environments around oil rigs, necessitating the development of a passive pressure sensor-based object detection system.

1.2 Challenges

Research in the field of Microelectromechanical Systems (MEMS) led to the creation of silicon-based millimeter-scale pressure sensors (Figure 1-3). These sensors consist of a pressure-concentrating diaphragm with a piezoresistive strain gauge patterned on the diaphragm's edge. A differential pressure across the diaphragm causes strain in the strain gauge which can be measured through its change in resistance. Silicon MEMS pressure sensors have been widely adopted because of their impressive linearity and high sensitivity. Additionally, integration with Complementary Metal-Oxide Semiconductor (CMOS) processing technology has allowed these devices to be batch-fabricated at low cost with integrated signal conditioning and offset-cancelling circuitry [5, 21].

However, while silicon is an ideal substrate for sensing air pressure, it is challenging to adapt it for the lateral line application because silicon wafer substrates are brittle and likely to fracture when mounted on the exposed hull of an aquatic vehicle. Making the silicon substrate conform to the vehicle's curved hull presents an additional challenge. In addition, silicon is chemically vulnerable to the corrosive seawater environment.

Attempts to construct a lateral line made of individual off-the-shelf silicon-based pressure sensors are limited in their spatial resolution and are difficult to mount on the exterior of the aquatic vehicle without protruding significantly and causing drag. The approach taken in [7] is to house the pressure sensors internally and route their pressure inlets to holes in the hull via tubing. However, this approach becomes more difficult if a pressure reading is desired from a location too small to internally house a sensor, such as the leading edge of a foil.

This thesis addresses these issues by constructing the pressure sensor array entirely from silicone elastomer materials, allowing the array to be waterproof, chemically protected, and flexible. The array is designed to have minimal thickness so that it may be mounted externally without affecting the streamlined structure of the aquatic vehicle's hull. Realizing this array requires the development of a new flexible material set, including a conductive elastomer to function as the pressure sensitive element.

In addition to being fabricated entirely from elastomers, the pressure sensor must also achieve the 10 pascal pressure resolution required by the lateral line application [7], while being able to withstand large absolute pressures on the order of several tens of kilopascals, due to the depth of the sensors below the surface of the water. Unfortunately, polymer and elastomer-based pressure sensors have typically been unable to achieve high pressure resolution due to the drift and hysteresis inherent in the viscoelastic behavior of polymer materials [8]. Thus, limiting the viscoelasticity and accounting for it with modeling and signal processing is another major challenge this work addresses. Section 3.1 summarizes the design requirements for the pressure sensor set by the lateral line application.

1.3 Prior Work

This section surveys existing works which have similarities to the flexible underwater pressure sensor array described in this thesis. Existing tactile sensors, flow sensors, and highly sensitive elastomer-based pressure sensors are considered and compared. The unique strengths of this thesis' approach to realizing the lateral line application

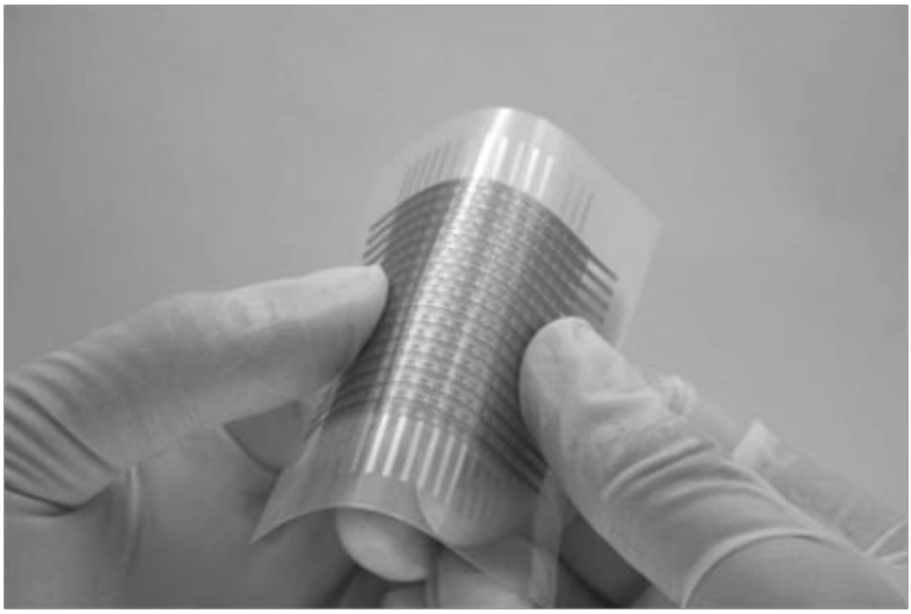

Figure 1-4: Picture of a flexible tactile sensor array [22].

are stated.

1.3.1 Tactile Sensor Arrays

Prior work involving large-area pressure sensor arrays has concentrated on tactile pressure sensing [22, 14], which has a very low pressure sensitivity requirement compared to that of the lateral line application. Tactile sensors are designed for applications where direct contact with an external object occurs. Often in these applications, simply knowing whether or not contact has been made is of more interest than the magnitude of applied pressure.

Many works have endeavored to find and characterize new conductive polymer materials capable of transducing a strain into a resistance change, while also being chemically and mechanically compatible with a flexible substrate. However, these works have also generally concentrated on tactile sensing, and therefore the resulting devices do not have adequate sensitivity for the lateral line application. [12] describes a pressure sensor which uses a carbon fiber sliver as the strain gauge for a polydimethylsiloxane (PDMS) diaphragm-based pressure sensor. The pressure versus strain gauge resistance transfer curve of the sensor is measured at 6 discrete

points, each spaced 5 kilopascals apart in pressure. Consequently, this sensor does not demonstrate the required 10 pascal resolution.

Several other pressure sensor works using novel polymer materials have also been designed for much higher amplitude pressure signals. [27] documents the development of pressure sensors using a carbon black-PDMS material similar to the composite used in this thesis. However, since they are intended for a tactile sensing application, the sensors do not make use of a pressure-concentrating diaphragm, and are thus much less sensitive. [9] presents a pressure sensor with the transduction element made of a carbon nanotube/polyimide (CNT/PI) composite, while [23] uses single-walled carbon nanotubes. Similarly to [12], the responses of all these sensors are characterized only at discrete pressures spaced 10 to 100 kilopascals apart. Consequently, they do not demonstrate the required 10 pascal resolution

Aside from single, discrete pressure sensing devices, work has also been done to create a flexible tactile sensing array [22], which is shown in Figure 1-4. Characterization of the 2-dimensional array is performed by pressing a rubber object against the array, generating a peak pressure of over 30 kilopascals. While the array is of interest to humanoid robotics, it is not designed for the lateral line application where small pressure variations on the order of 10 pascals are of interest, and there is no direct contact between external objects and the sensor.

1.3.2 Flow Sensors

Currently, the approach researchers have taken to create artificial lateral lines is to use an array of flow sensors rather than pressure sensors to interrogate the local fluid dynamics. [29] demonstrates the operation of MEMS-based flow sensors to characterize the hydrodynamic wake generated by an object moving underwater.

However, though MEMS flow sensors have adequate sensitivity for the lateral line application, they are very fragile since the sensor structure is based around a tiny artificial cilium made of silicon. Figure 1-5 diagrams one such flow sensor which is composed of an artificial silicon cilium with a resistive strain gauge at its base. As such, the device is vulnerable to having the silicon cilium fracture when under

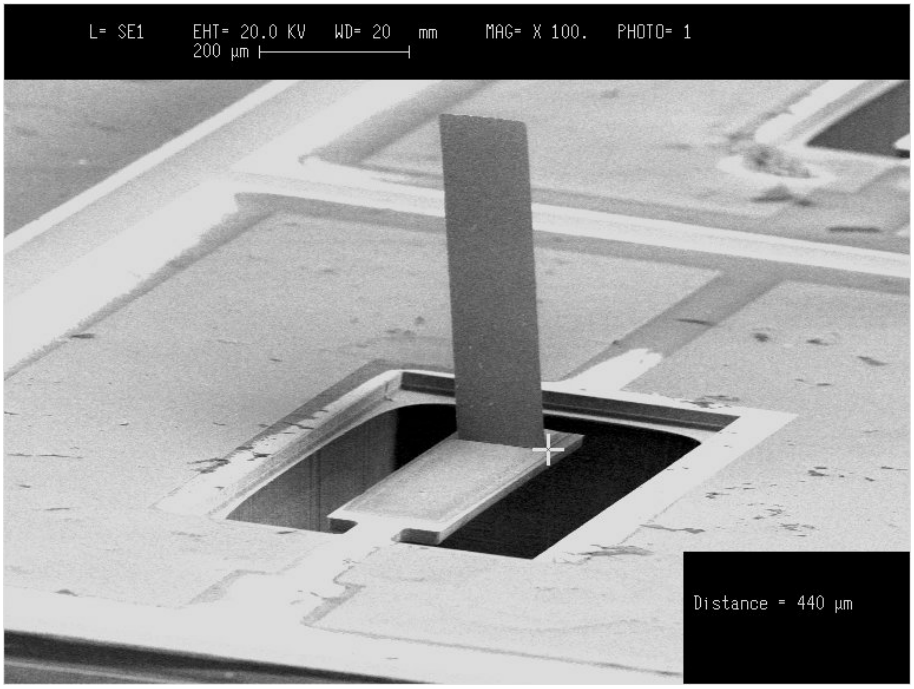

Figure 1-5: Scanning Electron Microscope (SEM) image of the MEMS flow sensor described in [6]. The vertical silicon cilium is 820x100x10 μm in dimensions.

high flow [6]. Additionally, in order to function underwater, the silicon substrates and strain gauges used in the flow sensors must be protected from oxidation and corrosion. Both [29] and [6] use paralyne to waterproof and protect the flow sensor arrays. However, the thickness of the parylene layer must be balanced between the competing concerns of electrochemical protection, and sensitivity [6].

1.3.3 Elastomer-Based Pressure Sensors

One very recent article describes a single pressure sensing device based around a silicone-and-carbon-nanotube (CNT) strain gauge composite patterned onto a PDMS diaphragm [13]. The article states that the CNT-PDMS pressure sensor is designed for high sensitivity, though no particular application is presented. While that material set and sensor design appears at first to be very similar to the carbon black-PDMS pressure sensors described in this thesis, there are several shortcomings in the design and experimental characterization of that CNT-PDMS sensor.

First, the CNT-PDMS sensor's claimed sensitivity of sub-10 pascals is only sup-

ported by an experiment where the pressure is ramped from 0 to 3 kilopascals and the CNT strain gauge's resistance is recorded every ∼5 pascals. This data is presented as a static characterization, since the sensor output is never shown as a function of time. While a single pressure ramp is sufficient to characterize highly linear silicon MEMS pressure sensors, it is insufficient to characterize the CNT-PDMS sensor because that sensor is made up of viscoelastic materials. These materials experience significant creep and stress relaxation, especially at the extremely large diaphragm displacements pictured in the article (several orders of magnitude greater than the thickness of the diaphragm). Those effects would cause the pressure-resistance transfer curve of the sensor to vary considerably from cycle to cycle. The CNT-PDMS sensor article does not mention viscoelasticity or any of its effects.

This thesis addresses viscoelasticity by performing thorough characterization and modeling of the sensor's dynamic response to both small and large-amplitude pressure signals. Hysteresis due to viscoelastic effects is significantly reduced by limiting diaphragm deflections to less than the diaphragm thickness.

1.3.4 Summary of Prior Work

The existing body of work in the area of flexible polymer-based pressure sensor arrays is geared towards tactile sensing applications where an object comes into contact with the sensor and generates a large pressure signal in the tens to hundreds of kilopascals. MEMS-based flow sensor arrays have been used for the lateral line application which requires a 10 pascal resolution, which is outside of the range that tactile sensors are capable of. However, these flow sensors are fragile and rigid because they use a silicon substrate and have protruding cilia. Thus, the flexible silicone-based pressure sensor array described in this thesis is the first polymer-based pressure sensor array designed to be both sensitive enough to interrogate the surrounding fluid dynamics, and rugged enough to be used in in the underwater environment for the lateral line application.

1.4 Research Goals and Contributions

The goal of this research is to enable passive underwater object detection and flow sensing by developing an artificial lateral line made of an array of underwater pressure sensors which may be externally affixed to the curved hull of an aquatic vehicle. Listed below are key contributions of this work to pressure sensor array design and fabrication, as well as key experiments demonstrating the capabilities of this technology.

- Developed a set of flexible elastomer materials for use in the pressure sensor array. A carbon black-PDMS composite is optimized for use as a resistive strain gauge.
- Designed and fabricated a flexible pressure sensor array using the elastomer material set. The array comprises MEMS-based pressure sensor cells each with a 10 mm square diaphragm. A 4-point probe strain gauge increases the device's pressure sensitivity and desensitizes the device to strains and vibrations outside of the active area.
- Characterized and modeled the dynamic response of the pressure sensor array to both small and large-amplitude pressure signals. Demonstrated the sensor's ability to resolve air or water pressure signals with a maximum resolution of 1.5 pascals. Identified a linear region of operation.
- Demonstrated underwater operation of the flexible pressure sensor array externally mounted to a hull. The array successfully transduces pressure waves generated by vortices, surface waves, and nearby moving objects.

1.5 Thesis Organization

Chapter 2 focuses on the design and characterization of an elastomer material set for use in the flexible pressure sensor array. PDMS is chosen to be used as the waterproof, flexible substrate. A conductive carbon black-PDMS composite is developed for use

as a strain-sensitive material that is both chemically and mechanically compatible with the substrate. The material's electrical and mechanical properties are characterized. Fabrication techniques for patterning layers and defining structures with the silicone material set are described. Finally, a theory explaining the material's electrical behavior is proposed.

Chapter 3 describes the design and fabrication of a pressure sensor array using the elastomer materials set. This chapter begins with a survey of different pressure sensor device geometries. The requirements of the underwater object detection application are translated into design choices. A MEMS-based geometry is selected to maximize the device's linearity and pressure sensitivity while limiting hysteresis. Finally, the fabrication process is described.

Chapter 4 focuses on the characterization and modeling of the pressure sensor array. First, the pressure sensor array is characterized by applying dynamic test pressure waveforms to the array. This serves as a calibration step which determines the sensitivity and resolution of each pressure sensing cell. A model explaining the behavior of the sensor is presented, and used to describe how to best use the device while avoiding the hysteresis inherent in the silicone material. The model is also used to predict how device performance scales with size.

Chapter 5 presents experimental results which demonstrate the array's ability to transduce underwater pressure waveforms generated by moving objects and surface waves. The output of the sensors is shown to match the pressure waveforms predicted by theory.

Chapter 6 concludes the thesis, summarizes the performance attributes of the pressure sensor array, and provides directions for future research.

Chapter 2

Elastomeric Materials for Flexible Pressure Sensors

This chapter describes the development of a flexible elastomer-based material set for use in the pressure sensor array. First, polydimethylsiloxane (PDMS) is selected to form the substrate and mechanically active structures of the sensor. A model for the viscoelastic properties of the PDMS is verified and fit to experimental data. Next, a conductive carbon black-PDMS composite is experimentally characterized. The composite is selected for use as the resistive strain gauge in the flexible pressure sensor array due to its low stiffness and smooth, monotonic change in resistance in response to strain. Mechanisms for the composite's resistance change in response to strain are described, and fabrication techniques for patterning layers of this material are developed. The resulting composite material is ready to function as the strain gauge in the pressure sensor array.

2.1 An Elastomer Substrate

Elastomers, also known as rubbers, are amorphous polymers composed of long chains of monomers as shown in Figure 2-1. Each monomer is typically made of carbon, oxygen, and hydrogen. The individual chains are amorphously tangled with each other. As the elastomer is strained, these tangled chains reconfigure themselves to distribute

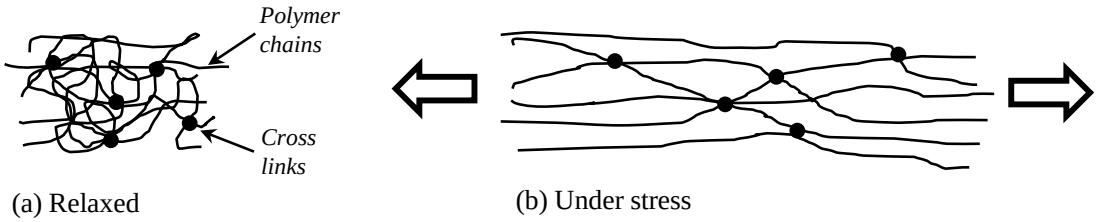

Figure 2-1: Conceptual diagram of an elastomer's polymer chains and crosslinks (a) in the relaxed state, and (b) upon applied stress.

the applied stress. Chemical bonds called "cross-links" exist between the chains and help the elastomer return to its initial state once the stress is removed. However, this process is not completely reversible as chains may change in conformation during the excitation, resulting in viscoelastic effects such as creep and stress relaxation.

Silicones form one subcategory of elastomers whose composition includes silicon in addition to the other elements. They have many useful properties including electrical insulation, waterproofing, and low chemical reactivity. As such, they can protect the electronically active components of the sensors, and are well-suited to withstand the corrosive underwater environment required by the lateral line application. PDMS is one such silicone widely used in MEMS with well-documented chemical, electrical, and mechanical properties [20], as well as well-developed micropatterning techniques [15]. For these reasons, PDMS is selected as the flexible substrate and structural material for the pressure sensor array.

2.1.1 Mechanical Response Model

For small strains, the dynamic response of a structure made of a viscoelastic material may be approximated as a linear time-invariant (LTI) system using the Burger model [8] shown in Figure 2-2. This model comprises a parallel dashpot c_P and spring k_P attached to a series dashpot c_S and spring k_S. The force-displacement transfer function of this model may be obtained from the constitutive equations of the system

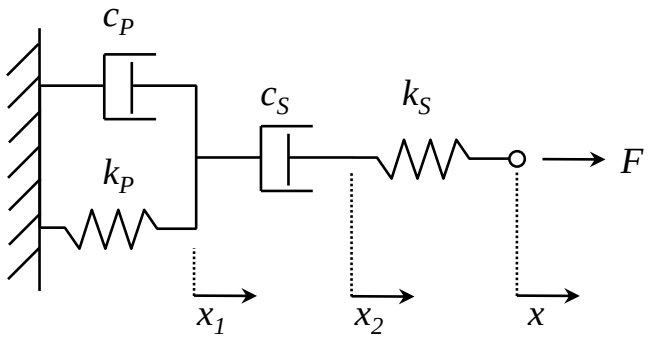

Figure 2-2: The Burger model approximates the stress-strain transfer curve $\frac{x}{F}$ of a viscoelastic material as an LTI system composed of springs and dashpots.

components, which include

$$F(t) = -c_S(\dot{x}(t) - \dot{x_2}(t)) \tag{2.1}$$

$$F(t) = -k_P x_1(t) - c_P \dot{x_1}(t) \tag{2.2}$$

$$F(t) = -k_S(x_2(t) - x_1(t)) \tag{2.3}$$

Equations 2.1-2.3 are combined to yield system's s-domain transfer function x/F. This transfer function may be considered the spring constant of the Burger model K_B, such that

$$K_B(s) = \frac{x(s)}{F(s)} = \frac{1}{k_P + sc_P} + \frac{1}{k_S} - \frac{1}{sc_S} \tag{2.4}$$

In order to verify the model and determine the values of the parameters, an experiment was performed to obtain force-displacement response data from the PDMS. As diagrammed in Figure 2-3, a Zwick mechanical tester was used to apply a cyclic displacement to the free end of a PDMS cantilever. The force-displacement relationship of a cantilever is governed by a spring constant K_C. Solid mechanics establishes a linear relationship between K_C and the tensile modulus of the material E, given by

$$K_C = \frac{EWH^3}{4L^3} \tag{2.5}$$

where W is the cantilever's width, H is its thickness, and L is its length [21]. Equating K_C to K_B shows that the intrinsic mechanical response of the material governed by

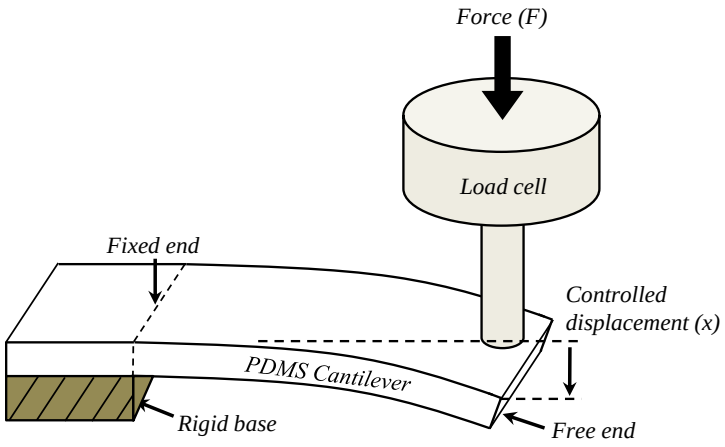

Figure 2-3: Diagram of experimental setup. The dynamic response of a PDMS cantilever 0.5 cm thick, 3 cm long, and 2cm wide is characterized using a mechanical tester.

E will be proportional to the response of the structure governed by K_B. Later on, the pressure sensor array will use a PDMS diaphragm which also has a spring constant that is proportional to E for small deflections. Thus, the PDMS diaphragm's force-displacement transfer curve will be of the same form as the transfer curve of the PDMS cantilever.

To determine the force-displacement relationship, a square wave of displacement is applied to the cantilever, and the corresponding force is recorded. The data is shown in Figure 2-4. The displacement data is fed into the Burger model to yield the simulated force, and the model parameters are tuned to have the simulated force match the measured force. The close match verifies that the model adequately captures the viscoleastic behavior of the PDMS.

Key features of the force and displacement waveforms are used to determine the values of the parameters in the Burger model. The peaking of the force in response to the displacement steps is due to stress relaxation, which may be modeled with a first-order system. This system is completely described by its initial value F_{init}, steady-state value F_{SS}, and time constant τ_P. Those three parameters will determine the values of k_P, c_P, and k_S. The fourth parameter c_S accounts for the slow downward drift in the force data, but it may be ignored while determining the other three parameters because c_S does not significantly compress during the time scale of force

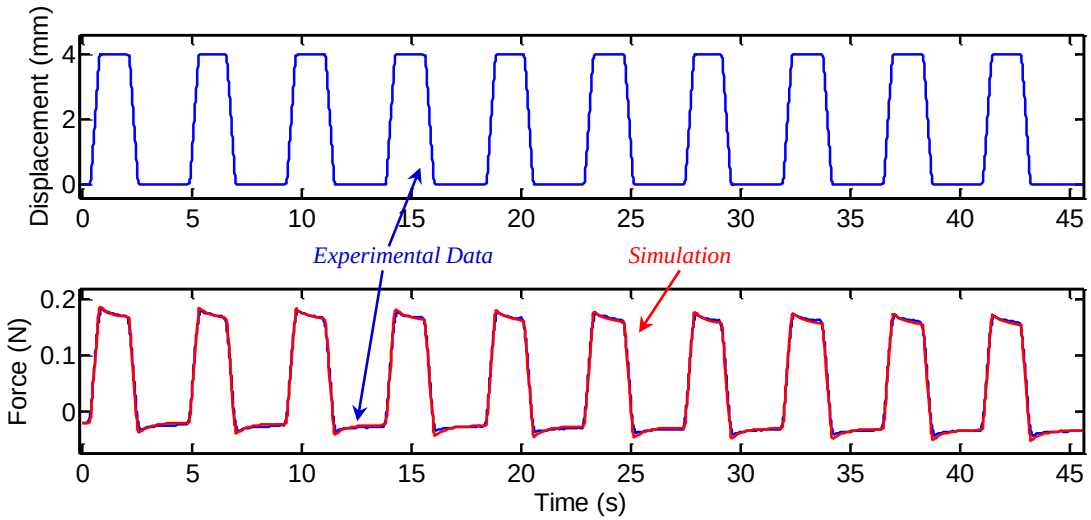

Figure 2-4: Dynamic response of cantilever showing applied displacement (top) and measured force compared to simulated force using the Burger model (bottom). Due to the good match, the simulated force (red) and measured force (blue) curves are difficult to distinguish.

peaking.

At the first displacement step, the relationship between F_{init} and the displacement x is given by

$$F_{init} = k_S x \tag{2.6}$$

because both dashpots c_P and c_S are incompressible during the edges of the displacement steps. The force reaches its steady state value F_{SS} when c_P stops exerting force. At this point, the system looks like the series combination of k_S and k_P, as described by

$$F_{SS} = \left(\frac{1}{\frac{1}{k_S} + \frac{1}{k_P}}\right)x \tag{2.7}$$

$$= (k_S||k_P)x \tag{2.8}$$

The || notation denotes the reciprocal of the sum of the reciprocals of the arguments, and is commonly used in circuit theory.

Next, the time constant of the stress relaxation may be obtained by finding the homogenous solution of the system consisting of the parallel components k_P and c_P.

This system is described by the relation

$$F = k_P x + c_P \dot{x} \tag{2.9}$$

Setting F to zero and solving for x yields

$$\tau_P = \frac{c_P}{k_P} \tag{2.10}$$

where τ_P is the stress relaxation time constant of the parallel components.

Using equations 2.6, 2.7, and 2.10, the parameters k_P, c_P, and k_S may be determined. The last parameter c_S is responsible for the the steady downward drift in the force data in Figure 2-4. c_S compresses due to the net positive displacement applied to the cantilever for the duration of the experiment. At this large time scale, c_P exerts insignificant force and may be ignored. This reduces the system to the series combination of c_S, k_S, and k_P, which is described by

$$F = k_S x = k_P x = c_S \dot{x} \tag{2.11}$$

The homogenous solution of this series system contains the series time constant τ_S, given by

$$\tau_S = \frac{c_S}{k_S || k_P} \tag{2.12}$$

This time constant is observable from the force data in Figure 2-4 as the slope of the force's downward drift, and may be used to solve for c_S.

2.1.2 Consequences for the Pressure Sensor Application

Using the methods outlined in Section 2.1.1, the Burger model parameters are obtained from the force-displacement data and listed in Table 2.1. These parameters are used to create the simulated force plotted in Figure 2-4. The very good match between the simulated and measured force curves validates the Burger model.

Figure 2-5 contains a bode plot made with the fitted parameters, depicting two key

Parameter	Value
k_S	54 N/m
c_S	6000 Ns/m
k_P	350 N/m
c_P	200 Ns/m
τ_P	0.57 s (f_P = 0.28 Hz or 1.76 rad/s)
τ_S	128 s (f_S = 0.0012 Hz or 0.008 rad/s)

Table 2.1: Values of Burger model parameters used in simulation shown in Figure 2-4. The corresponding time constants are also listed.

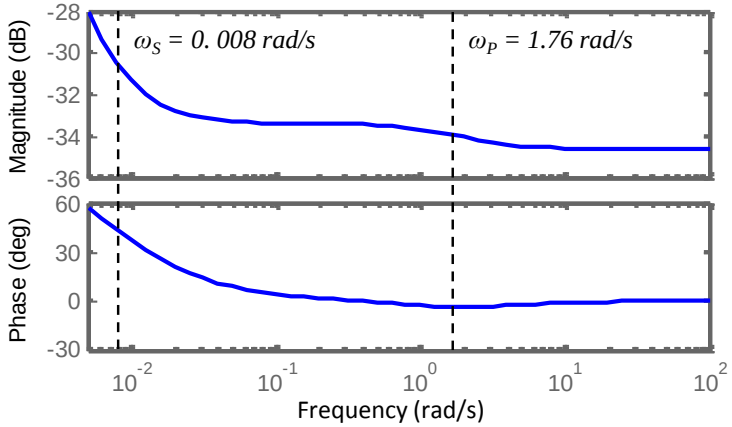

Figure 2-5: Bode plot of the Burger model transfer function $\frac{x}{F}$. Corner frequencies are emphasized.

corner frequencies of the PDMS mechanical response created by the time constants τ_P and τ_S. The corresponding frequencies f_P and f_S have important consequences for the pressure sensor application, since the PDMS will be used as the stress-to-strain transduction material for the sensor. Pressure signals slower than f_S cause the PDMS cantilever to creep. As the pressure frequency approaches zero, the strain response goes to infinity, which would result in a broken PDMS structure. In reality, the strain does not increase forever as the LTI Burger model would suggest, because the model only holds for small strains. Instead, the PDMS eventually reaches steady state and the creep stops. However, limiting the absolute pressure that the PDMS experiences helps reduce the magnitude of the creep. This will lead to the pressure equilibration scheme described in Chapter 3.

For pressure signal frequencies faster than f_P, the mechanical response will be governed solely by k_S since both c_P and c_S have stiffened at this frequency. For

frequencies between f_S and f_P, the PDMS cantilever's mechanical response will be governed by $k_P||k_S$, since c_S is only significant at longer time scales, and c_P is only significant at shorter time scales. However, because k_P is much greater than k_S, there will only be slightly more strain for an applied pressure. Thus, it is fair to approximate the PDMS cantilever's response as simply k_S for all frequencies faster than f_S.

In order to apply this model to PDMS structures other than the cantilever, we must extract the PDMS's tensile modulus E from k_S. Substituting k_S for K_C in Equation 2.5 gives

$$k_S = 54\ N/m = E \cdot \frac{2\ cm}{4} \cdot (\frac{0.5\ cm}{3\ cm})^3 \tag{2.13}$$

This relation yields $E = 2.35\ MPa$, which is close to the value of $E = 1.7\ MPa$ presented in [20].

In summary, for any pressure signal faster than f_S, stress relaxation is not a significant effect, so the entire mechanical response of the PDMS cantilever may be modeled as the spring constant k_S, and by extension, the PDMS may be modeled with the tensile modulus E. This will be the most desirable frequency range of operation for our sensor.

2.2 A Conductive Elastomer Strain Gauge

This section discusses the development of a resistive strain gauge material which is mechanically and chemically compatible with the PDMS substrate. Ultimately, a thin layer of this strain gauge material will be patterned onto a PDMS structure. Ideally, this material's tensile modulus should be smaller or similar to that of the PDMS, so that it would not inhibit the PDMS's strain. The PDMS structure transduces pressure to strain, and the strain gauge transduces the strain into a resistance change. Ideally, the strain gauge material's resistance should be a strong, linear function of its strain.

2.2.1 Material Synthesis and Patterning

The strain gauge material is chosen to be a composite material made of an elastomer doped with conductive filler particles. This choice immediately satisfies the requirements for conductivity, and chemical and mechanical compatibility with the PDMS. Several potential elastomer-conductive filler composite materials have been explored in the literature, including a nickel-silicone composite [2], and a carbon black-PDMS composite [1]. While both composites vary considerably in their electrical and mechanical characteristics, their syntheses involve the same process of uniformly dispersing the conductive filler particles within the elastomer's matrix, and then fixing them in place by curing the elastomer. The carbon black-PDMS composite is the focus of this section due to its smooth and repeatable strain-resistance relation.

To form the carbon black-PDMS composite, PDMS is prepared by pouring its two viscous liquid components into a mixing cup. Cabot XC-72 carbon black powder is poured into the cup to give a ratio of 1:6 carbon black:PDMS by mass. Because the powder is very light, it is measured by volume, given its density of 1 gram per 15 milliliters. The cup containing the PDMS and carbon black powder is then put into a Kurabo Mazerustar planetary mixing machine. The machine operates by spinning the cup, which uniformly disperses the conductive filler. The resulting mixture is a paste due to the high conductive filler loading.

A high concentration of filler improves conductivity at the cost of giving the paste a higher viscosity. Very high filler concentrations will cause the carbon black-PDMS paste to fail to cure. Very low concentrations will result in a non-conductive composite material. For the strain gauge application, the ratio of carbon black to PDMS was selected to provide a sheet resistance in the tens of kilohms to reduce power dissipation, and to provide the mixture with a pasty consistency so that it retains its shape during the patterning process.

Figure 2-6 diagrams the screen patterning process. The screen is made from an overhead transparency 100 μm in thickness. A milling machine removes material from the screen in the shape of the desired pattern. The screen is placed on top of the

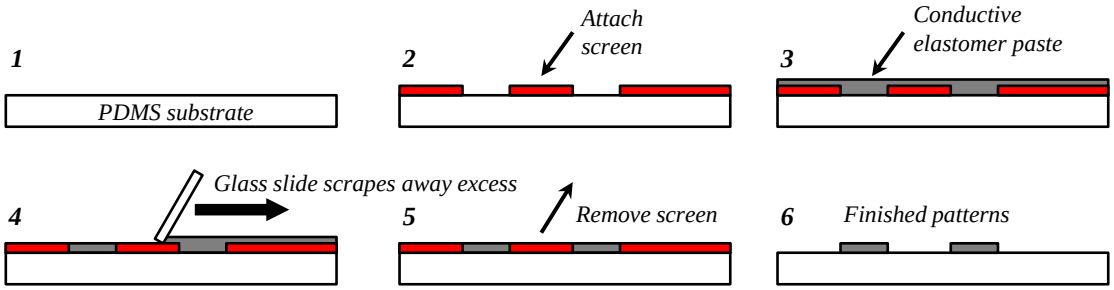

Figure 2-6: Process flow for the screen patterning of the strain gauge materials.

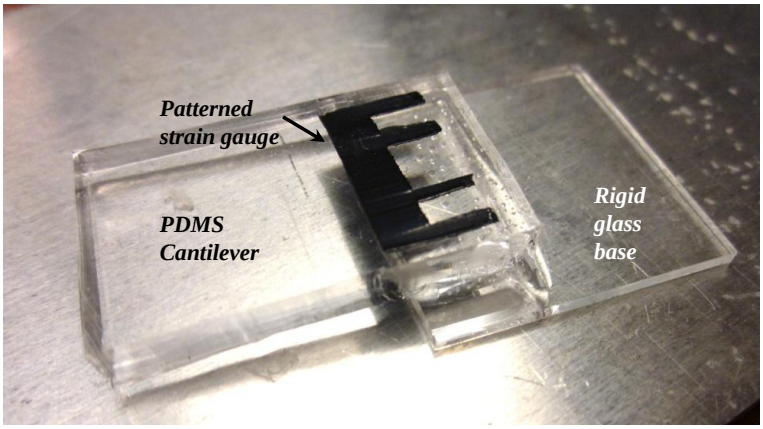

Figure 2-7: Photograph of the completed carbon black-PDMS strain gauge patterned onto a PDMS cantilever.

PDMS substrate, and the carbon black-PDMS paste is spread over the screen, making contact with the substrate in the locations of the screen that were milled away. A glass slide is swept across the screen, removing the excess material. The screen is then removed, leaving a 100 μm thick layer of the carbon black-PDMS paste in the shape of the desired pattern. The entire device is then cured on a hotplate at 120 ^{o}C for 10 minutes. Figure 2-7 shows a completed, patterened carbon black-PDMS strain gauge located at the base of a PDMS cantilever.

The screen is removed prior to the curing process to prevent the carbon black-PDMS mixture from becoming attached to it, and to prevent warping of the PDMS substrate due to thermal expansion mismatch. The mixture is capable of retaining its shape without the screen due to its pasty consistency set by the high filler particle concentration. The high temperature is used to flash cure the mixture while the filler particles are still uniformly dispersed; over time, gravity and Van der Waals forces will cause the mixture to dehomogenize.

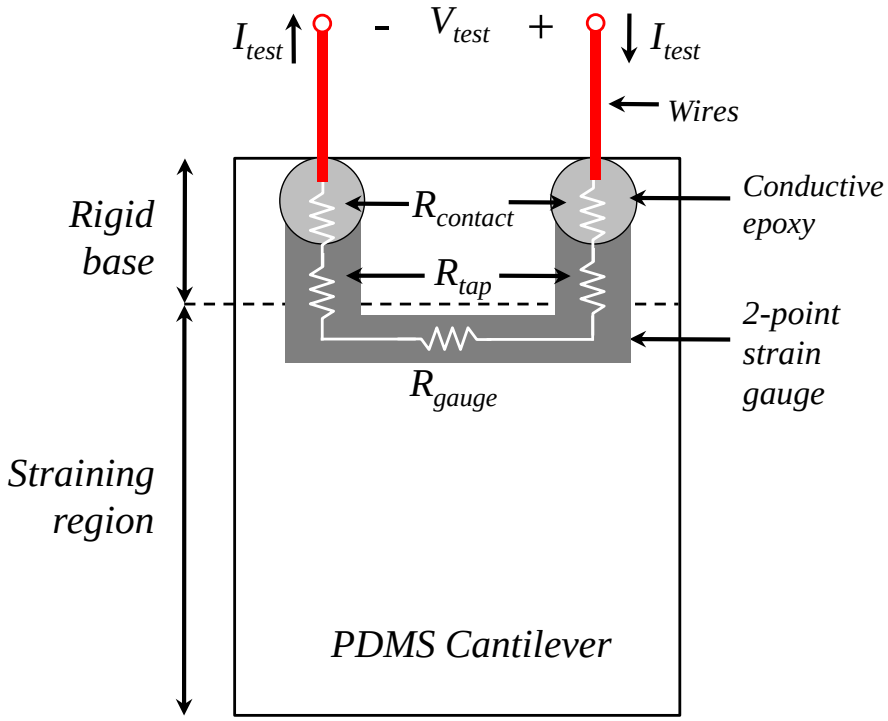

Figure 2-8: Diagram of a 2-point-probe strain gauge on the PDMS cantilever.

While the patterns used in this thesis have features on the millimeter scale, further miniaturization is possible with the screen printing technique. A laser-cut screen is used in [13] to pattern a CNT-PDMS conductive elastomer composite, yielding 50 μm-scale features.

2.2.2 4-Point-Probe Strain Gauge

The most straightforward method to use the composite material as a strain gauge would be to pattern a strip of the composite material onto the structure of interest, and connect two wires to it using conductive epoxy, creating a 2-point-probe setup. A current I_{test} could be passed through the wires, and the voltage V_{test} could be measured across the wires. Figure 2-8 diagrams a 2-point-probe strain gauge patterened onto the base of PDMS cantilever. The base of a cantilever is the region that experiences the greatest strain during deflection of the free end [21], so it is an ideal location for the strain guage.

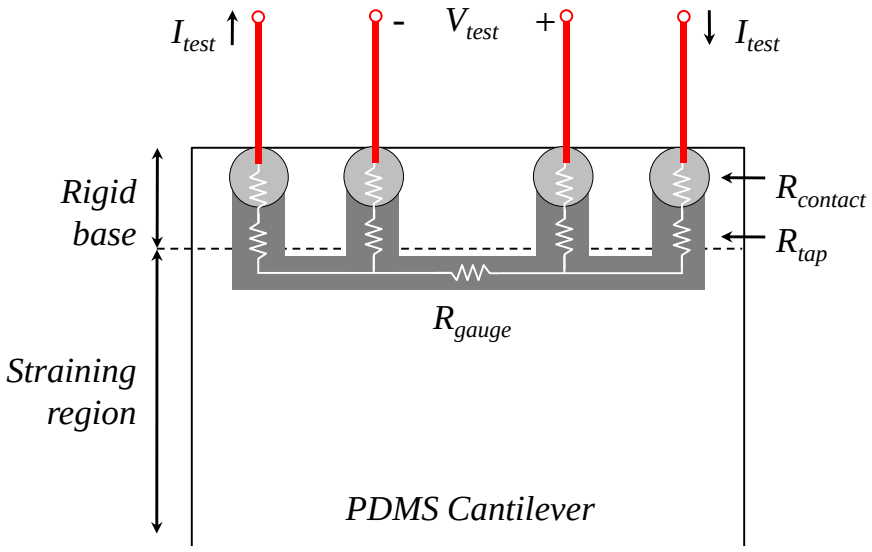

Figure 2-9: Diagram of the 4-point-probe strain gauge on the PDMS cantilever.

There are two substantial problems with using the 2-point-probe setup. First, a significant contact resistance $R_{contact}$ exists between the metal contact and the strain gauge resistor of interest R_{gauge}. Second, the metal contacts cannot be routed onto the PDMS cantilever because the strain would cause them to fracture. Thus, the conductive elastomer must be routed off the cantilever, which adds additional series resistances R_{tap}. The 2-point-probe measurement is only capable of measuring the sum of all series resistances, such that

$$R_{measured} = \frac{V_{test}}{I_{test}} = R_{contact} + R_{gauge} + R_{tap} \tag{2.14}$$

The extra sum terms reduce the sensitivity of $R_{measured}$ to changes in R_{gauge}. For dissimilar materials such as metal and silicone, $R_{contact}$ can be very high, as discussed in Section 2.2.3.

The 4-point-probe, alternatively known as a Kelvin structure, is shown in Figure 2-9. This structure solves the contact resistance problem because it allows for measurement of R_{gauge} alone, without being affected by series resistances $R_{contact}$ or R_{tap}. A constant current I_{test} is passed through the two current terminals while the voltage V_{test} is measured across the two voltage terminals. Since no current passes through the voltage terminals, no voltage appears across the $R_{contact}$ and R_{tap} on the voltage

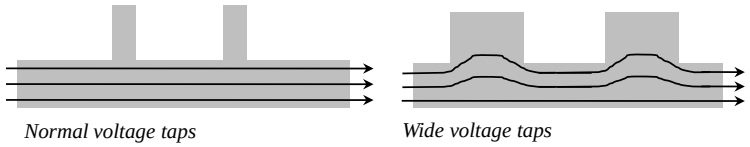

Figure 2-10: Illustration of the impact of voltage tap width on the current streamlines.

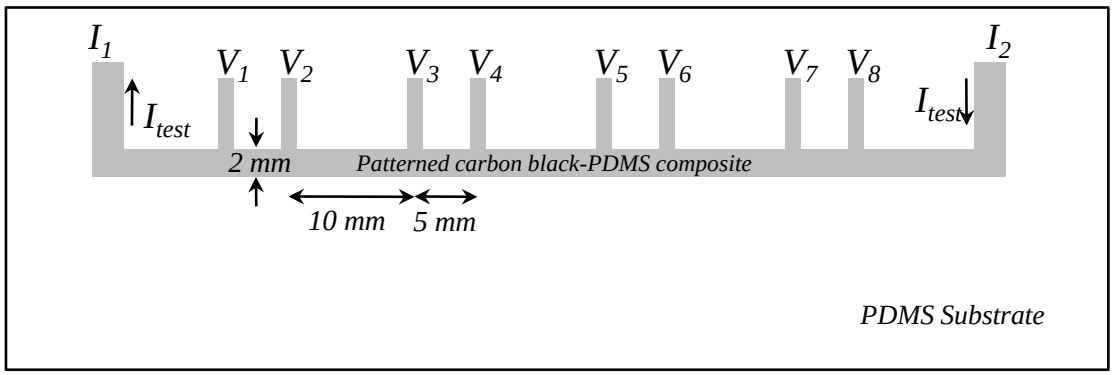

Figure 2-11: Diagram of experimental setup for measuring contact resistance, and variation in sheet resistance.

terminal branches, meaning that V_{test} is purely the voltage across the resistor R_{gauge}. Thus,

$$R_{measured} = \frac{V_{test}}{I_{test}} = R_{gauge} \tag{2.15}$$

Dimensions of the voltage terminals and current branch are chosen to keep the effective width of the current branch as uniform as possible over its entire length. A very wide voltage tap would provide additional paths for current flow, as illustrated in Figure 2-10 . Current flowing through these paths on the voltage terminals would interfere with the 4-point-probe measurement.

2.2.3 Sheet and Contact Resistance

Both the sheet resistance and the contact resistance of the 100 μm-thick patterned carbon black-PDMS composite are characterized using a variation of the 4-point-probe structure diagrammed in Figure 2-11. Instead of having 2 current terminals and 2 voltage terminals, 8 voltage terminals are used so that the sheet resistance of the patterned composite may be measured at different locations along the length of the current branch. This 10-point-probe structure will later be used to construct the

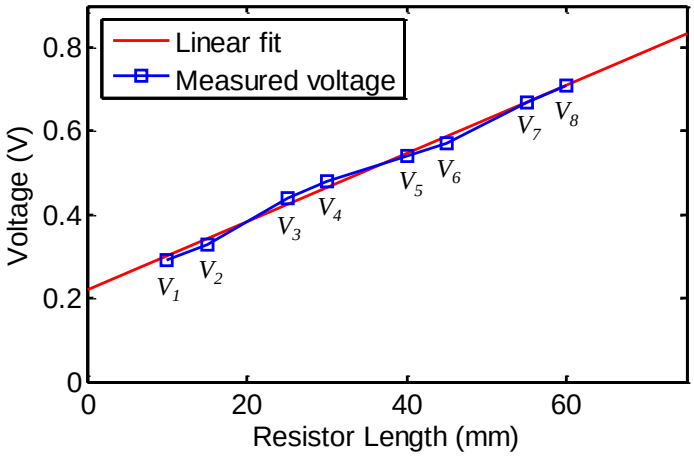

Figure 2-12: Voltage plotted against resistor length, with $I_{test} = 19\mu$A. Each voltage is measured with respect current terminal I_1.

pressure sensor array described in Chapter 3.

A 19 μA current is passed from I_1 to I_2 through the current branch. Voltages are measured from terminal I_1 to each of the other voltage terminals. The measured voltages are plotted against the length of the effective resistor (the distance between the terminals) to produce the plot in Figure 2-12. The linear fit of the data points demonstrates that the patterning process is capable of producing a patterned layer with a uniform sheet resistance. The fit is described by

$$V = 0.0082 \ \frac{\text{Volts}}{\text{mm}} \cdot L + 0.22 \text{ Volts} \tag{2.16}$$

where L is the length of the resistor. Dividing by I_{test} yields the resistance R, which is related to $R_{contact}$ and the sheet resistance R_S by

$$R = R_S \cdot \frac{L}{W} + R_{contact} \tag{2.17}$$

where L and W are the length and width of the resistor. Solving for R_S and $R_{contact}$ yields

$$R_S = 860 \ \Omega \tag{2.18}$$

$$R_{contact} = 11.6 \ k\Omega \tag{2.19}$$

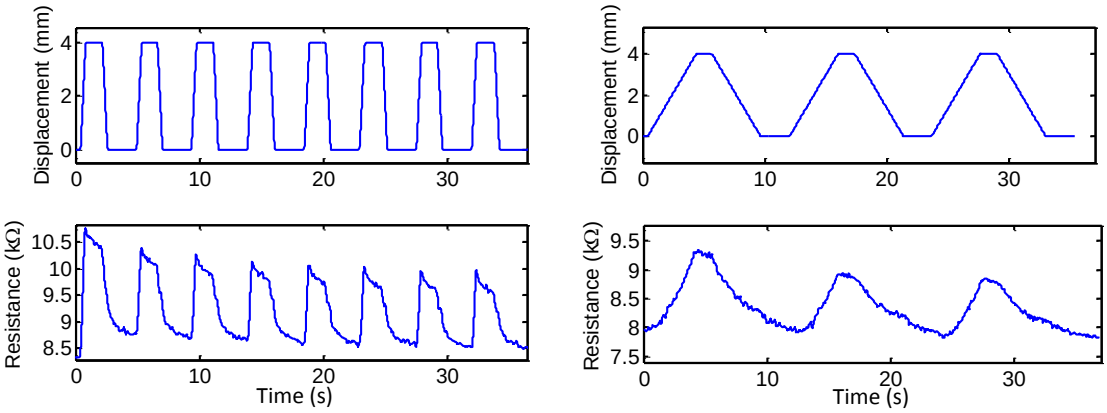

(a) Response to square wave of strain

(b) Response to triangle wave of strain

Figure 2-13: Dynamic response of the carbon black-PDMS composite's resistance to applied strain.

The nonzero y-intercept of the linear fit represents the contact resistance at the I_1 terminal. Because the contact resistance is much greater than the sheet resistance of the composite, using the 4-point-probe is essential to improve the sensitivity of the strain gauge.

2.3 A First Look at the Strain-Resistance Dynamic Response

The carbon black-PDMS composite is patterned to form a 4-point-probe strain gauge at the base of a PDMS cantilever as diagrammed in Figure 2-9. The goal of this experiment is to obtain the strain-resistance relationship of the composite. By design, the layer of the composite is much thinner than the PDMS cantilever, such that it doesn't significantly affect the cantilever's stress-strain relationship; it is assumed that the composite's strain follows the strain of the PDMS.

This section describes the initial investigation into the strain-resistance dynamic response of the carbon black-PDMS strain gauge, using a cantilever as the test structure. Mechanical excitation is performed with a Zwick machine, just as in the PDMS stress-strain tests diagrammed in Figure 2-3. The displacement of the free end of the cantilever is controlled with the Zwick machine, while the resistance of the strain

gauge is measured. The applied displacement and measured resistance are plotted in Figure 2-13. The response to a square wave of compressive strain is plotted Figure 2-13(a), while the response to a triangle wave of compressive strain is plotted in Figure 2-13(b).

The resistance waveform follows the rising and falling edges of the strain waveform, as desired. However, the rate at which the resistance increases upon applied strain appears greater than the rate at which it returns to its initial resistance after removal of the strain. This behavior will be further investigated and modeled in detail in Chapter 4, using pressure-resistance data taken from the completed pressure sensor array. For now, theories explaining the qualitative behavior of the composite are presented in the Section 2.4.

2.4 Mechanisms for the Resistivity Change

It is currently believed that the carbon black particles sinter together inside the elastomer matrix to form conductive chains which provide macroscopic conductivity to the carbon black-PDMS composite [4]. A large strain causes fractures in these chains, resulting in an immediate increase in the composite's resistivity. Upon removal of the strain, the decrease in the resistance back to its initial value is slower because the fractured chains must rely on Van der Waals forces to reconnect. This matches the qualitative features of the data in Figure 2-13.

However, if the applied strain is small enough in magnitude, it is possible that the carbon black chains would simply bend rather than fracture and reform. The greater reversibility of this mechanism would result in a resistance change with a smaller variation but a greater linearity to the applied strain. It is common in circuit design and MEMS devices to operate transistors and mechanical transducers within a small region of the full transfer curve to increase linearity. Chapter 4 demonstrates the linear strain-resistance response of the carbon black-PDMS composite when it is operated in the small-signal regime around a fixed operating point.

2.5 Summary

PDMS is selected as the substrate and as the structural material that will form the pressure-to-strain transduction element of the pressure sensor array. Its viscoelastic dynamic response is characterized and modeled as an LTI system with one significant corner frequency f_S at 2.7 milliHertz. Below this frequency, pressure signals cause the PDMS to creep. Above this frequency, the PDMS's mechanical response may be modeled with the tensile modulus $E = 2.35$ MPa.

A carbon black-PDMS composite is selected as the conductive elastomer strain gauge material. The conductive carbon black filler particles are uniformly dispersed in the PDMS, and form macroscopic conductive chains upon curing. A thin layer of the material is patterned in the shape of a strain gauge at the base of a PDMS cantilever using a screen patterning technique. The strain gauge uses the 4-point-probe concept to increase sensitivity, bypass the contact resistance, and allow the fragile metal leads to contact the composite off of the straining region of the cantilever.

The cantilever is mechanically and electrically characterized to determine the carbon black-PDMS composite's strain-resistance dynamic response. The rate at which the composite's resistance increases upon applied strain is greater than the rate at which it returns to its initial resistance upon removal of the strain. It is thought that large strains result in breaking of the conductive carbon black chains, while only Van der Waals forces act to reconnect the chain fragments when the strain is removed. It is further postulated that a small enough strain should cause a resistance change due to bending, rather than breaking, of the carbon black chains. The greater reversibility of the bending should improve the linearity of the strain-resistance dynamic response, as is demonstrated in Chapter 4.

Chapter 3

Design and Fabrication of the Pressure Sensor Array

Following the development of the carbon black-PDMS material set in Chapter 2, the next step is to proceed with the the design and fabrication of the flexible underwater pressure sensor array. Each pressure sensing cell in the array uses the typical strain gauge-on-diaphragm structure used in silicon MEMS pressure sensors. The PDMS is used as the material comprising the sensor's substrate and the pressure-concentrating diaphragm. The carbon black-PDMS composite is patterned onto the diaphragm and transduces its strain into a resistance change. The specific packaging and sensivity requirements set by the lateral line application are examined and used to design the sensor's geometry. Finally, the sensor's fabrication process is described.

3.1 Lateral Line Application Requirements

The lateral line application aims to use the pressure sensor array as a sensing strip externally affixed to an aquatic vehicle's hull, as previously discussed in Section 1.1. The packaging issues such as flexibility and waterproofing have both been addressed with the choice of the PDMS-based material set. The array's thickness is limited by adopting a MEMS-based pressure sensor design, since MEMS are constructed with planar fabrication processes.

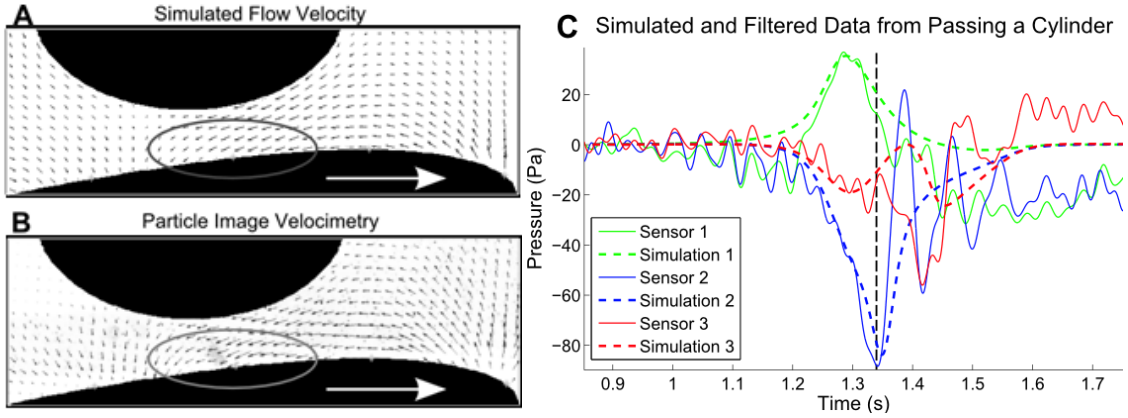

Figure 3-1: Pressure and flow data obtained from an aquatic test vehicle passing a ∼10 cm-diameter cylindrical rod at a distance of 1 cm. (A) Simulated flow field. (B) Measured flow field. (C) Measured pressure signals. Figure courtesy of [7].

The pressure sensitivity and spatial resolution are the two remaining requirements which dictate the dimensions of the mechanically and electrically active elements in the pressure sensor array. An experiment is performed in [7] where 3 commercially available discrete pressure sensors are mounted inside an aquatic test vehicle, spaced approximately 5 cm apart. Tubing is routed from the sensors to holes drilled in the hull so that the sensors measure the water pressure along the length of the vehicle. The vehicle is dragged at 0.5 m/s past a ∼10 cm-diameter cylindrical rod at a distance of 1 cm away. The pressure signals measured by the 3 sensors are on the order of 100 pascals in amplitude, and are shown in Figure 3-1. In order to clearly transduce features of this waveform smaller than the total amplitude, it is necessary for the pressure sensor array to resolve dynamic (AC) pressure signals on the order of 10 pascals.

Static (DC) spatial pressure distributions are also of interest to the lateral line application in situations such as the one depicted in Figure 1-1(a), where an object in a flow field generates pressure gradients of up to 1 kilopascal that vary spatially but are constant in time. However, it is important to note that the DC bias pressure is not of interest because it only represents the underwater depth of the vehicle. This pressure is relatively large, being 10 kilopascals at 1 meter underwater. The pressure equilibration scheme described in Section 3.2.3 is used to cancel out the DC bias,

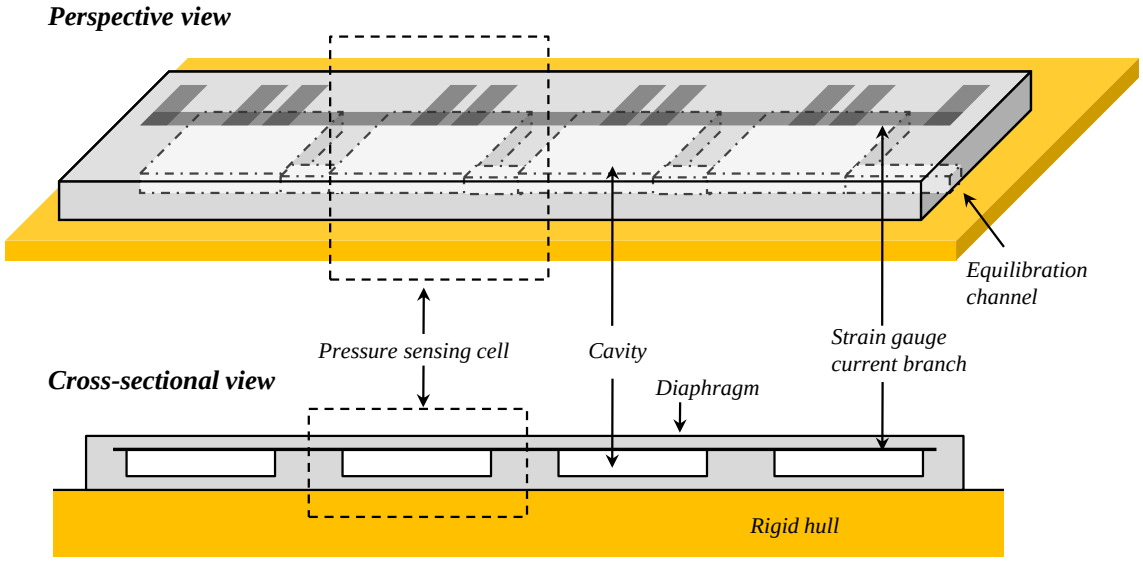

Figure 3-2: Diagram of the 4-cell pressure sensor array.

which would otherwise damage the thin diaphragm.

Finally, in order to query the shape of the object from the pressure data, it is necessary for the sensors to have a spacing smaller than the diameter of the object. This requires shrinking the lateral dimensions of the diaphragm, which unfortunately reduces the pressure sensitivity of the device. The pressure sensitivity and spatial resolution requirements are at odds and are balanced in the sensor design process.

3.2 Pressure Sensor Array Design

The pressure sensor array in this work consists of 4 pressure sensing cells as depicted in Figure 3-2. Each cell in the array is composed of three main active structures which are detailed in the following sections. The pressure-concentrating diaphragm is a thin square membrane made of PDMS which covers the pessure sensor's internal cavity. The diaphragm deflects in response to a pressure difference between the internal cavity and the environment. The 4-point-probe strain gauge made of the conductive carbon black-PDMS composite is patterned onto the underside of the diaphragm so that it is shielded from the water. Lastly, a pressure equilibration channel connects the cavities of all 4 pressure sensing cells to an external pressure reference.

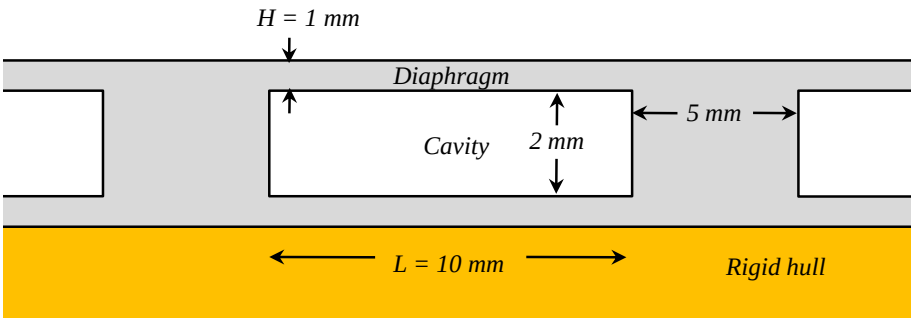

Figure 3-3: Cross-section view illustrating key dimensions of the PDMS diaphragms and cavities.

3.2.1 Pressure-concentrating Diaphragm

The dimensions of the diaphragm, given in Figure 3-3, are the main parameters that influence the pressure sensitivity of the device. For deflections less than the thickness of the diaphragm, the load-deflection behavior of a square diaphragm may be approximated by

$$P = \frac{\pi^4 E H^3}{6(1-\nu^2)L^4} \cdot c \tag{3.1}$$

where P is the pressure difference across the diaphragm, c is the deflection at the center of the diaphragm, H is the diaphragm thickness, and L is the side length of the square diaphragm [21]. ν is the Poisson's ratio, which may be approximated as 0.5 for PDMS since it is an elastomer. E, the tensile modulus, is approximated as 2.35 MPa, as determined in Section 2.1.2. Using Equation 3.1, the diaphragm dimensions may be chosen to keep deflection much smaller than the membrane thickness for pressures up to the maximum pressure of interest. Based on the pressure waveforms in Figure 3-1, 1 kPa is a generous upper pressure bound.

Since the focus of this thesis is not miniaturization, conservative dimensions are chosen for the sensor array. With $L = 10\ mm$ and $H = 1\ mm$, aluminum molds may easily be machined to create the cavity and membrane structure. For those dimensions, Equation 3.1 predicts a 0.2 mm deflection in response to a 1 kPa pressure. This deflection is smaller than H, thus achieving a self-consistent result. Theoretically, the depth of the cavity need only be large enough accomodate this deflection. However, the depth is chosen to be 2 mm to provide a large pressure reservoir. This way,

the volume change of the cavity due to diaphragm deflection is insignificant, which improves sensitivity.

This diaphragm will have a first resonance frequency f_0 based on its mass and spring constant, which may be estimated using the Rayleigh-Ritz method [30]. This gives

$$f_0 = 1.654 \cdot \frac{CH}{L^2} \tag{3.2}$$

where C is the speed of sound in the diaphragm material, H is the diaphragm thickness, and L is the diaphragm side length. C is related to the material parameters by

$$C^2 = \frac{E}{\rho(1-\nu^2)} \tag{3.3}$$

where E is the tensile modulus, ρ is the density of the PDMS, and ν is the poisson's ratio. Evaluating Equation 3.2 yields $f_0 = 940$ Hz. This number sets an upper bound on the bandwidth of the sensor. Realistically, viscous damping due to the water, air, and PDMS itself lower the sensor bandwidth. A bandwidth limit due to the carbon black-PDMS strain gauge's strain-resistance response would also be a possibility, though this does not appear to be the case based on results from the sensor characterization experiments of Chapter 4.

Lastly, the diaphragm center-to-center spacing sets the spatial resolution of the sensor. The spacing is chosen to be 15 mm which provides a 5 mm gap between the edges of adjacent diaphragms and prevents mechanical crosstalk. In comparison, sensor spacings on the order of 50 mm are used in the object identification and vortex tracking experiments performed in [7].

3.2.2 Strain Gauges

The PDMS diaphragm's deflection is transduced into a voltage using the 4-point-probe strain gauge design introduced in Section 2.2.2. The center of the diaphragm's edge experiences the greatest strain upon diaphragm deflection [21], so it is the ideal location for the strain gauge resistor R_{gauge}. As diagrammed in Figure 3-4, the four strain gauges share a common current branch that runs along the length of the array

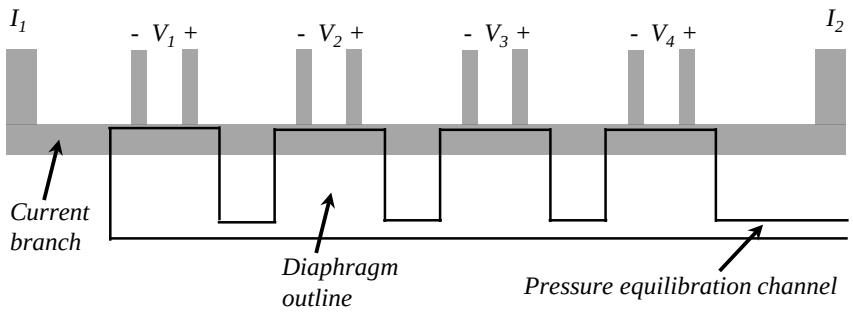

Figure 3-4: Top view illustrating strain gauge and alignment over the PDMS diaphragms. Dimensions are identical to those shown in Figure 2-11.

and is aligned with the edge of the diaphragm. Pairs of voltage taps are placed in each sensor cell to measure the resistance change at the center of the diaphragm's edge. By using a common current branch, the number of electrical connections required by the array scales with the number of sensors N as $2N + 2$. The dimensions of this four-strain-gauge composite structure are identical to the dimensions given in Figure 2-11 for the contact/sheet resistance experiment.

The strain gauges are patterned onto the underside of the PDMS diaphragm in order to shield them from the external environment. In the lateral line application, the seawater would short out the strain gauges if they were placed on the top of the diaphragm.

3.2.3 Pressure Equilibration System

As shown in Figures 3-2 and 3-4, the pressure equilibration channel connects all 4 cavities to an external port. A syringe may be connected to this port, enabling dynamic control over the cavity pressure. During characterization experiments, this allows for actuation of the diaphragms by changing the cavity pressure, as shown in Figure 3-5(a). For the lateral line application, a tube will run from the channel out into the water. The tube functions as a low-pass filter, so that the cavity pressure is set to the DC water pressure. This cancels the large DC bias pressure that would otherwise damage the sensors, while still allowing measurement of small-amplitude pressure signals in the frequencies of interest. Additionally, because all of the cavities

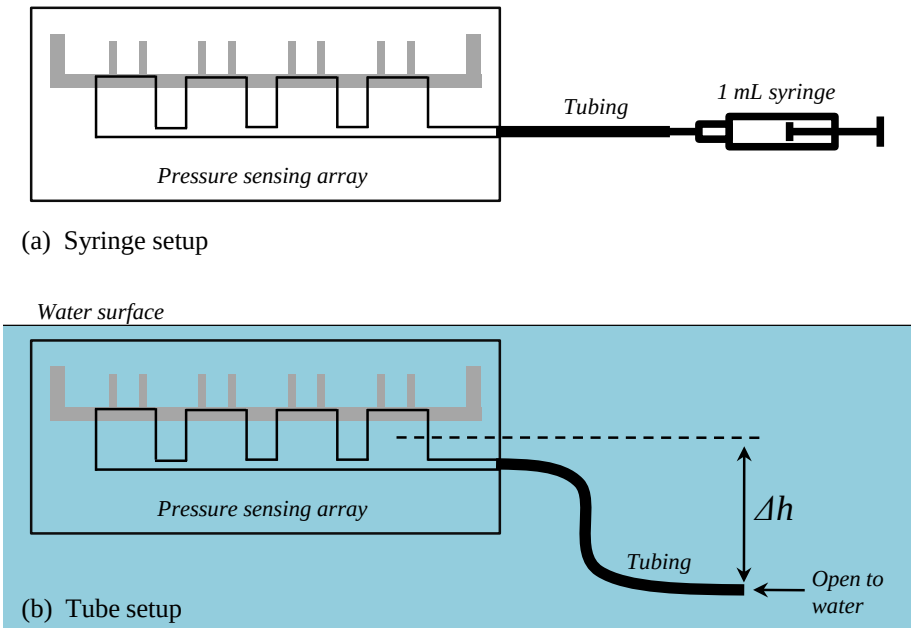

Figure 3-5: Diagram of pressure equilibration schemes. (a) Syringe setup used for characterization and testing. (b) Tube method used for underwater deployment.

share the same pressure, the array is still capable of transducing DC differential pressures between individual sensors, in contrast to underwater microphones which are incapable of transducing any DC pressure.

The difference in depth Δh of the end of the tube connected to the water and the depth of the diaphragms determines the differential pressure bias P_{bias} applied to the sensor cells, as shown in Figure 3-5(b). This pressure bias may be calculated as

$$P_{bias} = \rho g \Delta h \tag{3.4}$$

where ρ is the density of water and g is Earth's gravitational acceleration. The tube method allows for the DC differential pressure bias across the diaphragms to stay constant, independent of the depth of the sensors in the water. In Chapter 5, these pressure biasing techniques will be used to bias the strain gauges into tension for reasons described in Chapter 4.

3.2.4 Flexibility

The sensor may be mounted on a curved surface as long as the strain on the diaphragms induced by the curvature ϵ_{bend} does not exceed to exceed the maximum strain experienced by the diaphragms in the small-deflection regime ϵ_{max}. This maximum strain ϵ_{max} is given in [21] as

$$\epsilon_{max} = \frac{6}{\pi^2}(1-\nu^2)(\frac{L}{H})^2\frac{P}{E} \tag{3.5}$$

where P is the maximum differential pressure allowed across the diaphragm while keeping it well in the small-deflection regime, and is determined to be 1 kPa in Section 3.2.1. Equation 3.5 evalutes to $\epsilon_{max} = 0.02$.

ϵ_{bend} should be kept much smaller than ϵ_{max} so that it does not significantly affect the deflection of the diaphragm. ϵ_{bend} may be estimated as

$$\epsilon_{bend} = \frac{z}{R} \tag{3.6}$$

where R is the radius of curvature, and z is the radial distance from neutral axis to the plane of the array containing the diaphragms. The thickness of the sensor array is 3 mm, so the neutral axis is approximately at 1.5 mm, making $z \approx 1$ mm. Setting $\epsilon_{bend} = 0.1\epsilon_{max}$ yields a maximum radius of curvature of $R = 0.5$ m in which the flexible pressure sensor array would be able to operate normally. Section 4.6 presents experimental results in which the sensor is mounted on a curved hull and its performance is characterized.

3.3 Fabrication

Figure 3-6 diagrams the fabrication process. PDMS is cast in machined aluminum molds to form the 2 mm-thick cavity and channel structure, and two 1 mm-thick sheets. One of the sheets will form the diaphragms above the cavities, and the other will form the backplanes below the cavities. Using the screen patterning technique

shown in Figure 2-6, the carbon black-PDMS composite is patterned to form the strain gauges on the PDMS sheet that will form the diaphragms. 40-gauge (80 μm) copper magnet wires are bonded to the current and voltage terminals of the strain gauges using uncured carbon black-PDMS paste as a "conductive epoxy." The paste is cured at 120 ^{o}C to fix the wires in place.

A thin $\sim$100 μm layer of uncured PDMS is spread onto the top of the PDMS cavity/channel structure. This layer is used to bond the structure to the PDMS sheet containing the strain guages. In order to position the strain gauges at the edge of the diaphragms, the edge of the cavities opposite the channel is aligned with the edge of the strain gauge current branch. The cavity/channel structure is then pressed against the PDMS sheet containing the strain gauges. The entire device is baked on a hot plate at 120 ^{o}C for 10 minutes in order to cure the PDMS between the two layers.

The exposed side of the cavity/channel structure is bonded to the remaining 1 mm-thick PDMS sheet using the same process as the previous bond, with the $\sim$100μm layer of uncured PDMS applied to the exposed side of the cavity/channel structure. Finally, the device is placed diaphragm side-down into the recess of a rectangular aluminum mold. Additional uncured PDMS is poured into the mold, fully encapsulating the remaining exposed regions of the strain gauges and wires. The device is cured at 120^{o}C on a hot plate for 20 minutes. Photographs of the completed pressure sensor array are shown in Figures 3-7 and 3-8.

Overall, the diaphragms, strain gauges, and air channel are well-defined and cleanly-patterned. However, fabrication issues visible in the photographs include the messy appearance of the strain gauge terminal-to-wire bonds, and a few bubbles trapped in the PDMS structure from the final strain gauge encapsulation step. Despite the appearance, neither of these issues significantly impact the performance of the device. As long as the strain gauge terminals provide a conduction path to the wires, their specific geometry does not affect the 4-point-probe measurement of R_{gauge}, which is cleanly patterned. Also, the bubbles are not located near the mechanically active regions of the sensors.

The terminal-to-wire bonds may be improved by creating another screen to act as

a mask for the carbon black-PDMS paste that is used to bond to the wires. For the pictured device, the paste was applied with a swab. The bubbles were created from air trapped during the PDMS pouring step, and may be avoided by pouring more slowly.

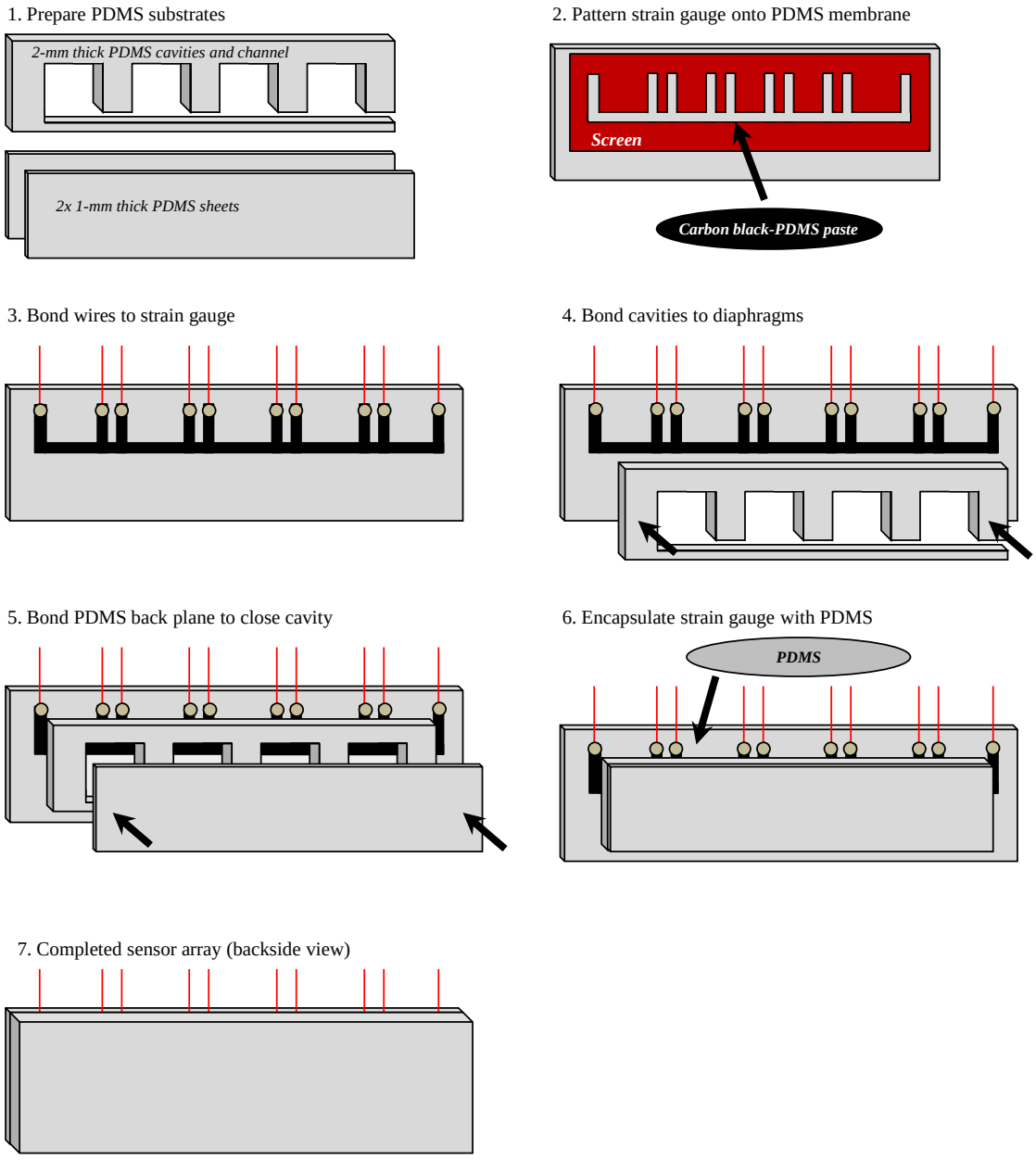

Figure 3-6: Process flow for the pressure sensor array.

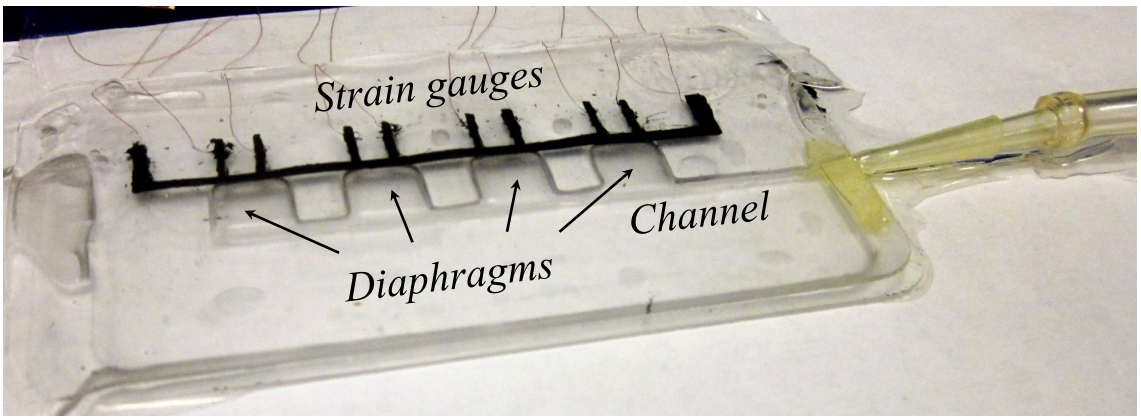

Figure 3-7: Photograph of finished pressure sensor array. The PDMS is transparent, so the array was placed on a piece of paper for this picture.

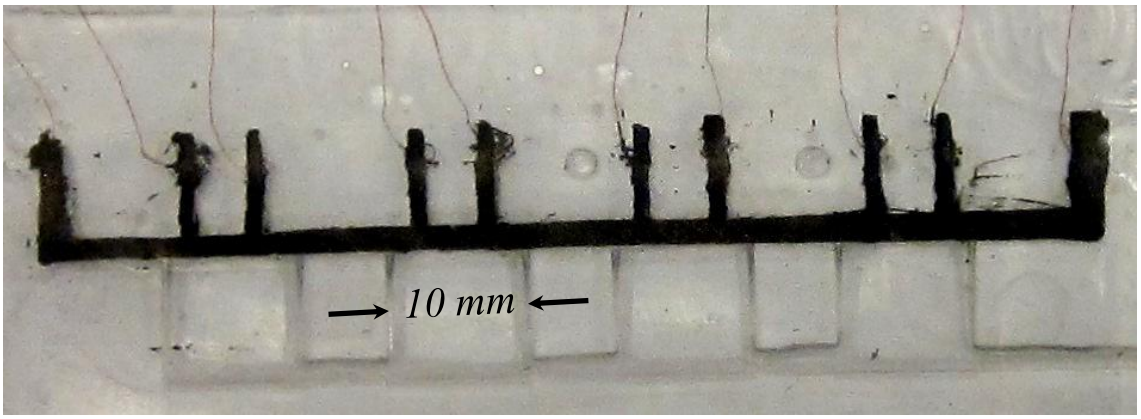

Figure 3-8: Close-up photograph of the active region of the pressure sensor array.

Chapter 4

Characterization and Modeling of the Pressure Sensor Array

The flexible pressure sensor array fabricated in Chapter 3 is dynamically characterized by applying small-amplitude pressure signals at several DC bias pressures up to 1 kilopascal. This mimics the conditions that the sensor is expected to experience when used for the lateral line application. The sensor output voltages, proportional to the strain gauge resistances R_{gauge}, are recorded. Finally, a numerical model relating the applied pressure to R_{gauge} is presented and is supported by the underlying physics of the diaphragm and strain gauge.

4.1 Measurement Circuit

As shown in Figure 4-1(a), a current source feeds a current $I_{src} = 19\mu$A through the I_1 and I_2 terminals of the array. The sensors are numbered 1-4. Each pair of voltage terminals V_1 through V_4 is connected to the differential input of an instrumentation amplifier which provides a gain of 9. The amplified output is passed through a 12 Hz first-order anti-aliasing filter. This filtered output is fed into a National Instruments USB-6215 16-bit analog-to-digital converter (ADC) and recorded at 1 kS/s. In order to remove 60 Hz pickup, a finite-impulse response (FIR) low pass filter [17] of order 100 with a 40 Hz brickwall cutoff is used. For the characterization experiments, the

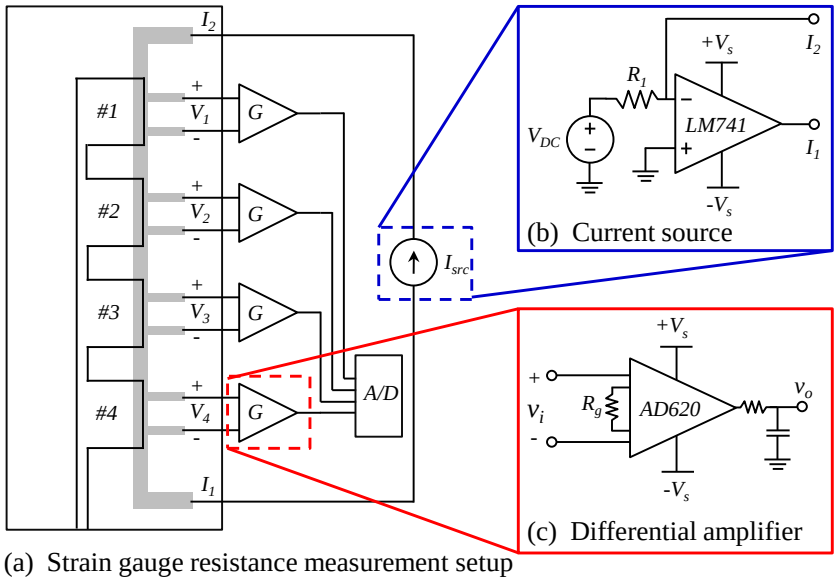

Figure 4-1: Diagram of measurement setup for the four-sensor array.

pressure signal bandwidth is kept below 10 Hz, so the 12 and 40 Hz corner frequencies are adequate.

The current source circuit, detailed in Figure 4-1(b), uses an LM741 op amp configured as an inverting amplifier. The current branch terminals I_1 and I_2 are placed in the feedback path. Supply voltages V_S provide ± 15 volts to the op amp. As long as the op amp output does not saturate at these supply rails, the current through the current branch may be considered constant. To create the 19 μA bias current, a constant voltage $V_{DC} = 5$ V is applied at the input, and the resistor R_1 is set to 265 kΩ.

Each voltage terminal pair is connected to the differential amplifier circuit shown in Figure 4-1(c). Four amplification channels are made for the four pressure sensing cells. The amplifier circuit consists of an Analog Devices AD620 instrumentation amplifier, using $R_g = 6.2$ kΩ to provide a gain of $G = 9$. The differential input v_i presents a 10 GΩ input resistance, which is desirable for the 4-point-probe measurement. Its single-ended output is fed into an 12 Hz first-order resistor-capacitor (RC) low pass filter with $R = 13$ kΩ and $C = 1$ μF. The output v_o of the filter is routed to the ADC.

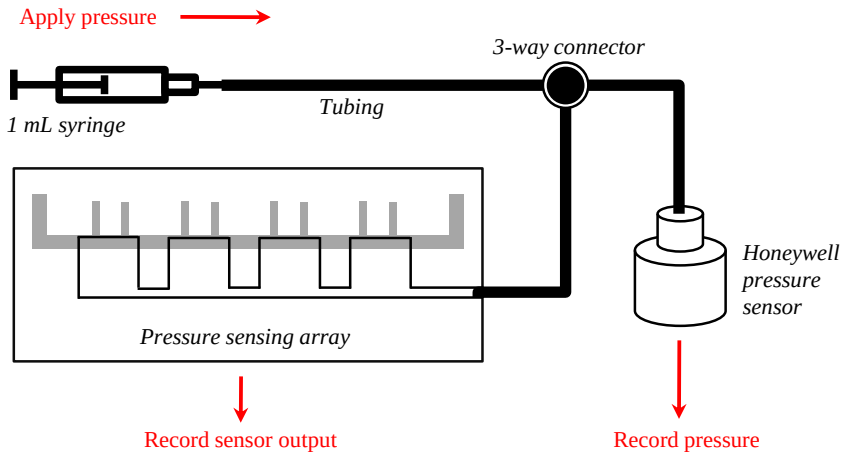

Figure 4-2: Diagram of characterization setup using air pressure to actuate the array.

4.2 Characterization via Air Pressure

Figure 4-2 diagrams the characterization experiment setup. The pressure sensor array is mounted to a rigid, flat backing using epoxy. A three-way connector links the pressure sensor array's channel to a commercial Honeywell 19C015PG4K pressure sensor [11] and a 1 mL syringe using tubing. This effectively creates a sealed chamber containing the syringe, the connective tubing, and the channel and cavities of the pressure sensor array. The actuation of the syringe modulates the pressure inside of the chamber. Because the same pressure is experienced by the commercial pressure sensor and the pressure sensor array undergoing testing, the array may be calibrated against the commercial pressure sensor. At the beginning of each test, the differential pressure across the sensor diaphragms is zeroed by setting the cavity pressure to the atmospheric pressure.

The convention used for this chapter's graphs is for the plotted pressure to be the pressure measured by the commercial pressure sensor with respect to atmospheric pressure. Thus, a positive pressure indicates that the cavity pressure is higher than the atmospheric pressure, causing the pressure sensor array's diaphragms to bulge slightly outwards. In this operating regime, the carbon black-PDMS strain gauge experiences tensile strain. All of the array testing experiments described in this thesis, including the underwater experiments, are preformed in the positive pressure regime

Sensor (#)	Resistance (kΩ)
1	31.6
2	31.7
3	30.1
4	33.3

Table 4.1: Initial resistances of the strain gauges of the four sensors at zero strain.

to keep the strain gauge in tensile strain. This chapter focuses on characterizing and modeling this operating regime because it is shown to be able to linearly transduce small-amplitude pressure signals. Sensor operation in neutral and compressive strain is not characterized in this thesis, though it is briefly discussed in Section 6.2.

Before applying any pressure, the initial resistances of each of the strain gauges at zero strain are determined using the measurement circuit and are given in Table 4.1. They are significantly higher than the value of 2.2 kΩ predicted by the sheet resistance determined in Section 2.2.3. This is likely due a combination of batch-to-batch fabrication variation and accidental excess bending and stretching of the flexible device during fabrication and testing. The excess strain would cause irreversible breaks in some of the conductive carbon chains, increasing the initial resistance of the strain gauges. However, the sensitivites of the strain gauges should not be affected, as the remaining carbon chains would still undergo the same fractional resistance change.

Next, two different test pressure waveforms are applied to the chamber with the syringe. The first pressure waveform, plotted in Figure 4-3(a), represents the differential pressure across all four diaphragms. This test pressure waveform consists of a superposition of small-amplitude, sinusoidal pressure waves on top of large-amplitude, symmetric rising and falling steps of pressure. The level that the pressure is held at after each step may be thought of as the operating point around which the small-amplitude pressure signal is applied. The voltage output measured from each of the four sensors is converted to resistance by dividing by I_{src}. This resistance R is normalized to R_0, the value of R at the start of the dataset. The normalized strain gauge resistance R/R_0 is plotted in Figure 4-3 for each sensor.

The theory behind the carbon black-PDMS composite's resistance change pre-

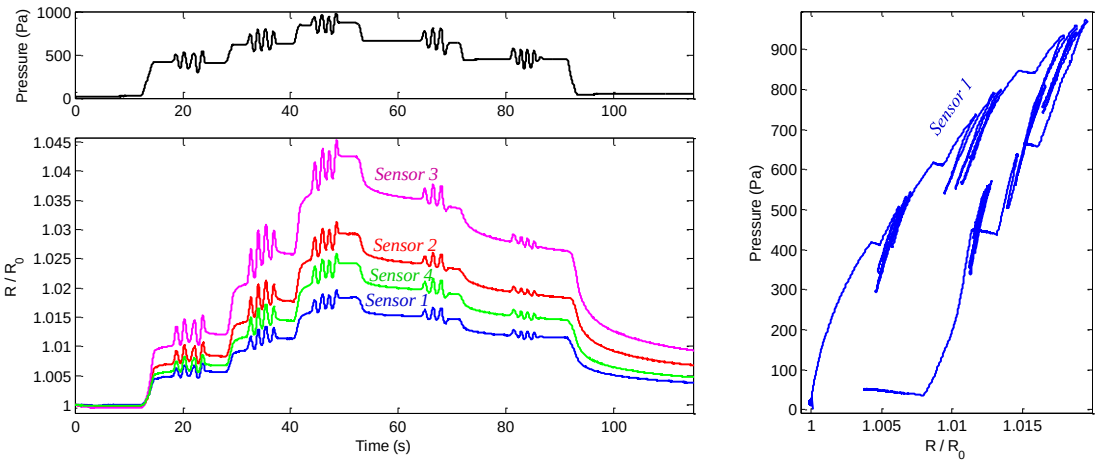

(a) Pressure and resistance waveforms for Sensors 1-4

(b) Transfer curve for Sensor 1

Figure 4-3: Multiple pressure step dynamic characterization data and transfer curve.

sented in Section 2.4 predicts a nonlinear strain-resistance response for large-amplitude strains, in which the composite's resistance is able to increase faster than it is able to recover and decrease to its original value. This is reflected in the dataset, where the levels of the falling R/R_0 steps are higher than the levels of the corresponding rising steps. The theory also predicts a more linear strain-resistance relationship for small-amplitude strains. From the dataset, it appears that the small-amplitude sinusoidal pressure signals are proportional to the small-amplitude resistance changes. However, this is difficult to confirm because the small-amplitude sinusoidal pressure was applied before the large-amplitude resistance step had reached steady-state, causing a superposition of the two behaviors.

Figure 4-3(b) plots the pressure waveform against the resistance waveform of Sensor 1 to obtain the large-amplitude transfer curve. This transfer curve shows that the resistance increases superlinearly as the pressure increases, and sublinearly as the pressure decreases. This is similar to the transfer curve of a damped spring system, and suggests there is damping behavior present in the large-amplitude response.

The second test waveform, shown in Figure 4-4, attempts to seperate the sensor's superposition of a nonlinear large-amplitude response and a linear small-amplitude response. The test begins with the chamber held at atmospheric pressure. A large-amplitude 500 pascal pressure step is then applied, followed by five cycles of a small-

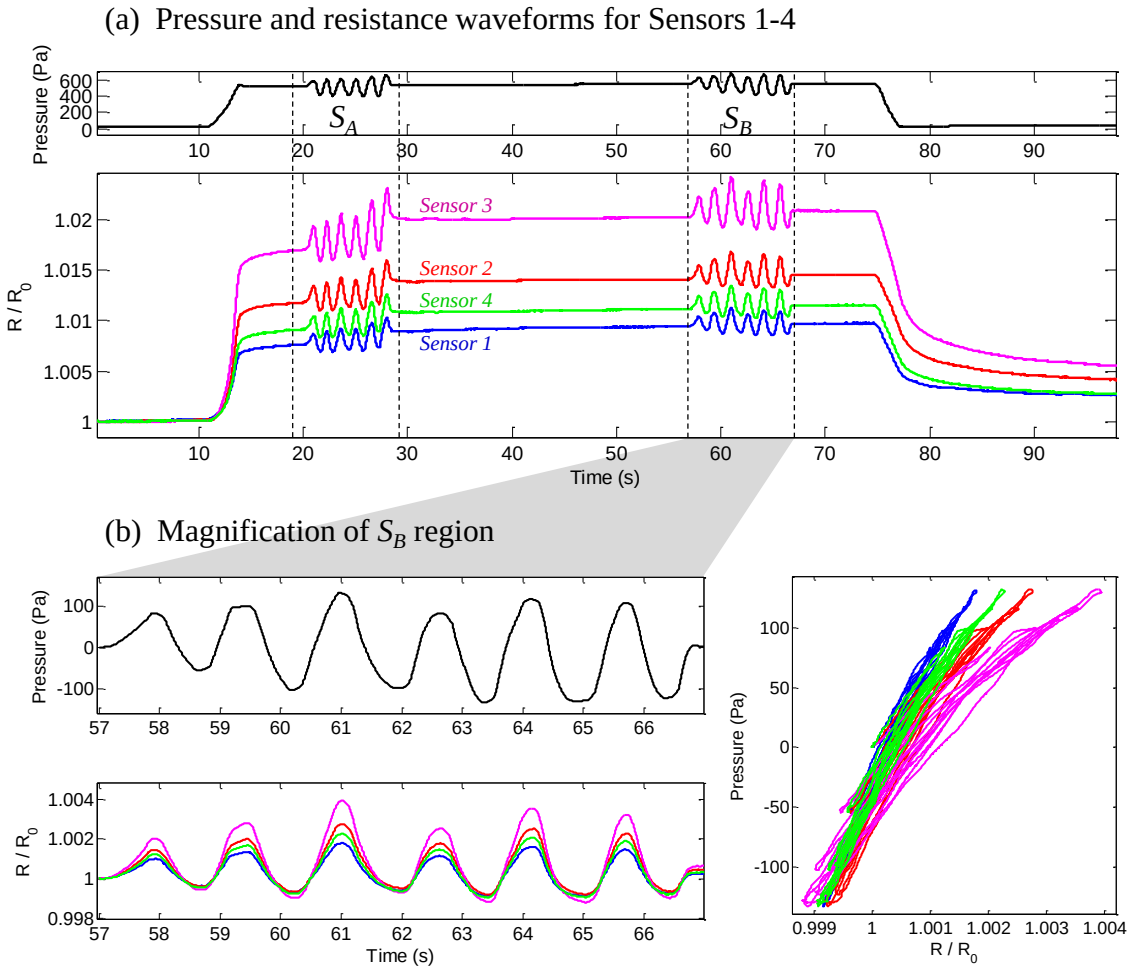

Figure 4-4: (a) Single pressure step dynamic characterization data illustrating the four sensors' responses to small-amplitude pressure signals S_A and S_B. (b) Time-domain magnification and transfer curves of small-amplitude sinusoid S_B re-normalized to the operating point of each sensor.

amplitude 200 pascal, 0.7 Hz sinusoid at that operating point, labelled as S_A. The operating point is held for 40 seconds to allow the strain gauge's resistance increase to reach steady state, after which six more cycles of the sinusoid are applied, labelled as S_B. The pressure is then stepped back down to atmospheric.

The strain gauge resistance responses of all four channels have the same form. S_A occurs before the large-amplitude resistance step has reached steady state, resulting in a superposition of the large and small-amplitude response. However, S_B occurs after steady state of the large-signal step has been reached. This allows the linearity of the small-ampliude response to be examined independently. Figure 4-4(b) uses the data

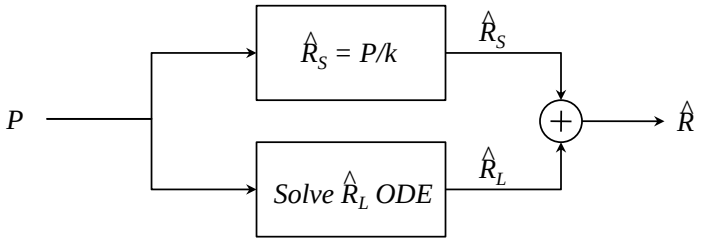

Figure 4-5: Block diagram of the numerical model of the pressure sensor response. The input P is the differential pressure across the diaphragm and the output $\hat{R}$ is the strain gauge's fractional resistance change.

from the S_B region and plots the pressure against the resistance to create transfer curves for each of the four sensors. The linearity of each transfer curve demonstrates the linear relationship between pressure and resistance for small-amplitude signals. The slope of each line represents the effective small-amplitude pressure sensitivity of each sensor in the array. The sensitivities of each sensor are are explicitly determined in Section 4.4.

In summary, the output voltage waveform of each of the array's four sensors is able to capture the major features of both test pressure waveforms, including large-amplitude rising and falling edges, and small-amplitude cyclic sinusoids. However, while the sensor's response to small-amplitude signals is linear, the large-amplitude response appears to be nonlinear and damped, producing asymmetry in its response to rising pressure and falling pressure.

4.3 Numerical Modeling

The numerical model presented in this section quantitatively captures the features of the sensor's pressure-resistance relationship previously discussed. This model is valid for the range of pressures that produces an outward deflection of the sensor's diaphragm that is smaller than the diaphragm's thickness. The outward deflection is necessary to operate the strain gauge in tensile strain, and the small-deflection limit prevents irreversible breaking of the conductive carbon strands in the strain gauge. This pressure range is satisfied by the lateral line application, where pressure biasing

techniques can be used to achieve the outward deflection, and the pressure waves of interest are smaller than 1 kPa, which only produces a 0.2 mm diaphragm deflection as calculated in Section 3.2.1.

As diagrammed in Figure 4-5, the model relates the differential pressure P across the sensor's diaphragm to the fractional change in resistance R/R_0 experienced by the strain gauge, written here as $\hat{R}$. The model consists of a nonlinear, time-invariant component representing the large-amplitude resistance response $\hat{R}_L$, summed with an LTI component representing the small-amplitude resistance response $\hat{R}_S$, such that

$$\hat{R} = \hat{R}_L + \hat{R}_S \tag{4.1}$$

The small-amplitude component $\hat{R}_S$ is linear, such that

$$\hat{R_S} = \frac{P}{k} \tag{4.2}$$

where k is the slope of the small-amplitude transfer curves shown in Figure 4-4(b).

The large-amplitude response $\hat{R_L}$ is described by a differential equation obtained from combining an expression describing the static component of the response with an expression describing the dynamic component. The static component describes the steady state response of $\hat{R_L}$ to a static pressure P_{static}, according to

$$\hat{R_L} = g_1 P_{static} + g_2 P_{static}^2 \tag{4.3}$$

where $\hat{R_L}$ is a quadratic function of P_{static} with coefficients g_1 and g_2. Equation 4.3 is based on the superlinear transfer curve shown in Figure 4-3(b). Because the nonlinearity is slight in the pressure range of interest, the particular form of the nonlinearity is not critical; for this empirical model it is only important that there exists a parameter for tweaking superlinearity in the curve-fitting process. Note that P_{static} need not be explicitly calculated from P, since it will later disappear during substitution.

Next, an equation governing the dynamics of the large-amplitude response is

Parameter	Value	Unit
g_1	$1 \cdot 10^{-6}$	Pa^{-1}
g_2	$1.2 \cdot 10^{-8}$	Pa^{-2}
c	600	$\text{kPa} \cdot \text{s}$
k	90	kPa

Table 4.2: Model parameters for Sensor 1 used for the simulations in Figure 4-6.

added. This "viscous" damping component is given by

$$P = c\frac{d\hat{R}_L}{dt} + P_{static} \tag{4.4}$$

where P is the differential pressure across the diaphragm and c is the damping coefficient. The $c\frac{d\hat{R}_L}{dt}$ term slows the rate $\hat{R}_L$ changes in response to P. Solving Equation 4.3 for P_{static} and substiting into Equation 4.4 and yields

$$\frac{d\hat{R}_L}{dt} = \frac{1}{c}(P - \frac{-g_1 + \sqrt{g_1^2 + 4g_2\hat{R}_L}}{2g_2}) \tag{4.5}$$

which is a nonlinear first-order differential equation in R_L.

Together, Equations 4.1, 4.2 and 4.5 comprise the model relating the differential pressure across the sensor's membrane to the normalized resistance change experienced by the strain gauge. This model is implemented in a MATLAB script included in Appendix A. The model parameters g_1, g_2, c, and k are fitted to the pressure-resistance response of Sensor 1, shown in Figures 4-3 and 4-4. The test pressure waveforms of both figures are then fed into the script to produce simulated resistance waveforms. Figure 4-6 compares the simulated resistance to the measured resistance for both of the tests. The same parameters are used for both simulations. Table 4.2 lists all of the model parameters for Sensor 1.

The simulated resistance closely tracks the measured resistance during the rising large-amplitude steps. However, the levels of the falling steps in the simulation do not correspond to the measured data quite as well. Nevertheless, the simulation still produces the asymmetric levels of the rising and falling steps. Since an LTI model would not be able to produce such an asymmetry, this demonstrates that the model

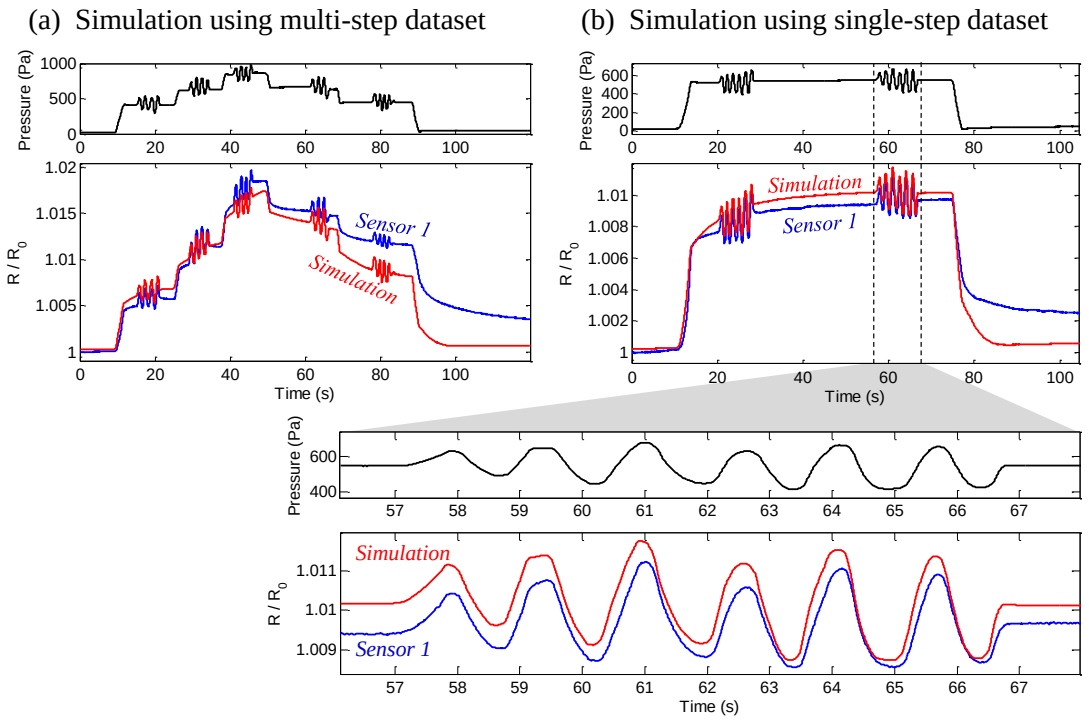

Figure 4-6: Comparison of simulated resistance to measured resistance in response to (a) the multi-step test pressure of Figure 4-3 and (b) the single-step test pressure of Figure 4-4.

requires the nonlinearity. Choosing a more optimal form of the nonlinearity would improve the fit of the large-amplitude steps. Overall, the correspondence between the simulated and measured resistance validates the concept of having a linear small-amplitude response superposed with a nonlinear, large-amplitude response.

4.4 Consequences for the Pressure Sensor Application

Ideally, a pressure sensor should have a linear correspondence between the applied pressure and the measured signal. Though this is not the case for the overall response of the elastomer-based pressure sensor array, the small-amplitude response of the array is indeed linear, as discussed in Section 4.3. If the nonlinear large-amplitude response is allowed to reach steady-state, then small-amplitude pressure deviations from that operating point will produce a linear response from the pressure sensor.

Sensor (#)	k parameter (kPa)	Sensitivity ($\Delta R/R_0$ per 100 Pa)
1	90	$1.1 \cdot 10^{-3}$
2	77	$1.3 \cdot 10^{-3}$
3	54	$1.9 \cdot 10^{-3}$
4	86	$1.2 \cdot 10^{-3}$

Table 4.3: Small-amplitude sensitivities of the four pressure sensors according to the data in Figure 4-4.

Fortunately, as described in Section 3.1, small-amplitude pressure deviations are the pressure signals of interest to the lateral line application. After the aquatic vehicle reaches its operating depth and the large-amplitude response reaches steady state, it is the small-amplitude pressure variations generated by objects near the vehicle that are of interest. In general, the smaller the amplitude of the pressure signal, the greater the linearity of the response.

The k parameter of the model is the effective small-amplitude sensitivity. Table 4.3 lists the sensitivities of each of the four pressure sensors, according to the data shown in Figure 4-4(b). The average small-amplitude sensitivity of the pressure sensors is a $1.38 \cdot 10^{-3}$ fractional change in resistance per 100 pascals, with a coefficient of variation of 0.25. Waveforms with this scale peak-to-peak resistance variation are readily measurable with a standard 16-bit ADC, which has quantization levels at $2 \cdot 10^{-5}$ fractional variation. Thus, the sensitivity of these pressure sensors is comfortably sufficient to resolve pressures at the 10 pascal level of interest to the lateral line application. In order to make use of the small-amplitude regime described by the model, the sensors must be operated in the positive pressure regime. This may be implemented with the tube or syringe pressure bias schemes described in Section 3.2.3.

The pressure sensors will also still be able to transduce DC pressure gradients between sensors according to the large-amplitude static pressure response described by Equation 4.3. In this case, the sensor output is single-valued but not linear with the pressure.

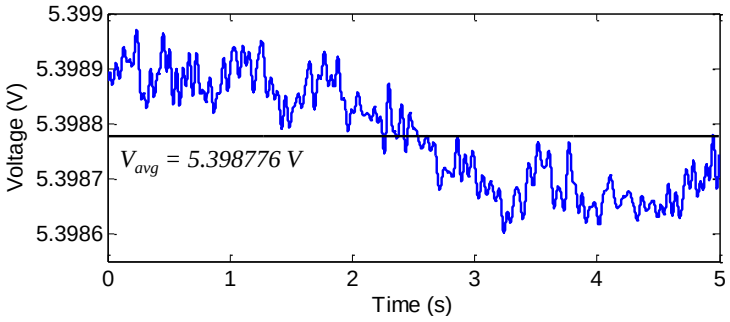

Figure 4-7: Plot of Sensor 1's amplified voltage output illustrating illustrating a 100 μV RMS noise voltage, which is a tiny fraction of the signal's operating point. This waveform was taken with a gain of 9 and $I_{src} = 19$ μA. The data has been low-passed with a 40 Hz FIR filter.

4.5 Pressure Resolution, Noise, and Power

In order to quantify the pressure sensitivity of the sensors, the noise voltage present in the sensor output must be measured. The measurement circuit described in Section 4.1 is slightly altered so that an 870 Hz RC low pass filter is used as the anti-aliasing filter, and the sampling rate is 10 kHz. An FIR filter of order 1000 with a brickwall cutoff frequency of 40 Hz is used to eliminate 60 Hz pickup. This increased bandwidth provides a more accurate sample of the noise spectrum. Figure 4-7 depicts the noise present in the voltage output of Sensor 1, using a gain of 9 and a 19 μA test current. The root-mean-square (RMS) voltage of the AC noise is 100 μV. Compared to the DC value of the signal, this is only a $2 \cdot 10^{-5}$ fractional variation.

Because 40 Hz is more than enough to accomodate the underwater pressure signals of interest to the lateral line application, the measured RMS noise voltage is an accurate rendition of the actual noise experienced in the application. Thus, the minimum fractional resistance variation $\hat{R}_{min}$ that the sensor is able to resolve is $2 \cdot 10^{-5}$. Combining this with the sensitivity data in Table 4.3 yields the pressure resolution for each sensor, given in Table 4.4.

Since $\hat{R}_{min}$ is on the order of the quantization levels of the 16-bit ADC, it is likely that the quantization error limits the pressure sensitivity. Aside from this bottleneck, other noise sources include pickup and thermal noise. Increasing the gain

Sensor (#)	Resolution (Pa)
1	1.8
2	1.5
3	1.1
4	1.7

Table 4.4: The pressure resolution of the sensors for a 40 Hz measurement bandwidth, based on the measured RMS fractional variation noise $\hat{R}_{min}$ and the sensitivity data in Table 4.3.

of the AD620 helps improve the signal power with respect to interference generated by pickup. The fundamental resolution limit of the pressure sensor itself is set by the thermal noise of R_{gauge}. A thermally-limited resistance measurement has an RMS noise voltage V_n of

$$V_n = \sqrt{4k_B T \Delta f \cdot R_{gauge}} \tag{4.6}$$

where k_B is Boltzmann's constant, T is the temperature and Δf is the bandwidth of the signals of interest. Since the pressure signals in the lateral line application operate on slow time scales ($<$ 40 Hz), limiting Δf to that bandwidth does not negatively affect the application. Evaluating this expression yields $V_n = 141$ nV, which is about 1000 times smaller than the measured voltage noise.

The signal-to-noise ratio (SNR) may also be improved by raising I_{src} at the cost of additional power consumption P_{sig}, though this is undesirable for energy-limited autonomous vehicle applications. An estimate of the power consumption of a single sensor is given by the power dissipated in R_{gauge}:

$$P_{gauge} = I_{src}^2 * R_{gauge} \approx 10\mu\text{W} \tag{4.7}$$

Note that the actual power consumption of the array is greater because I_{src} must flow through the entire current branch, not just the R_{gauge} portions. An estimate of the power consumption of the entire array is then given as

$$P_{array} = I_{src} * V_S \approx 285\mu\text{W} \tag{4.8}$$

which shows that much power is lost due to the contact resistance and current branch

(a) Array mounted onto a curved hull with a 0.5 m curvature

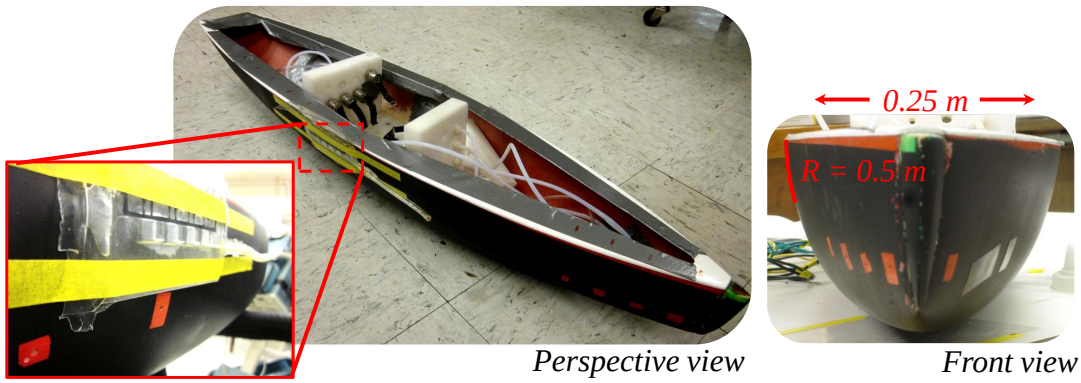

(b) Small-amplitude response of array while mounted on the curved hull

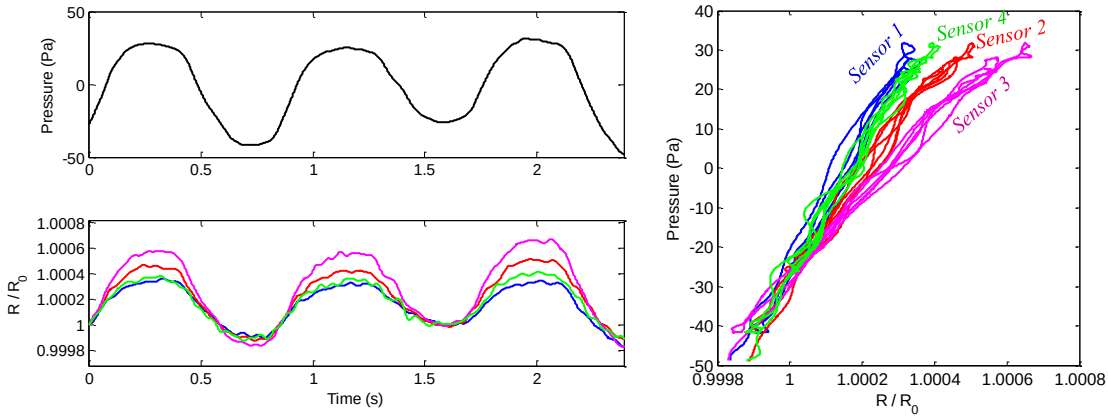

Figure 4-8: Photograph and results from the flexibility characterization experiment.

series resistances. However, compared to typical silicon MEMS pressure sensors with a 5 V supply and a 5 kΩ strain gauge resistance yielding a 5 mW power consumption per sensor [11], this pressure sensor array is very power efficient.

4.6 Characterizing the Flexibility

According to Section 3.2.4, the array should be functional while mounted on a curved hull with a maximum radius of curvature of $R = 0.5$ m. For this experiment, the array is mounted on a mockup AUV hull with an approximate curvature of 0.5 m, as shown in Figure 4-8(a). While mounted, a small-amplitude sinusoidal pressure is applied using the syringe, just as in the characterization experiments described in Section

Sensor (#)	Sensitivity ($\Delta R/R_0$ per 100 Pa)
1	$0.6 \cdot 10^{-3}$
2	$0.8 \cdot 10^{-3}$
3	$1.1 \cdot 10^{-3}$
4	$0.7 \cdot 10^{-3}$

Table 4.5: Re-calculated small-signal sensitivities for the four sensors when mounted onto a hull with a 0.5 m radius of curvature. Compare to Table 4.3.

4.2. The resulting time-domain data and small-amplitude transfer curve are plotted in Figure 4-8(b). The small-signal pressure sensitivities for each sensor are calculated from the slopes of the curves and are given in Table 4.5. These values are all slightly less than the sensitivities at zero curvature, given in Table 4.3. This is likely due to a slight stiffening of the diaphragm from the additional bending strain. Despite the altered sensitivity, the linearity of the small-amplitude response is preserved. Thus, the array is able to function while mounted on an AUV's curved hull, only requiring a re-calibration step after the mounting.

4.7 Limits of Scaling

Miniaturization of the pressure sensor's dimensions improves the spatial resolution of the array. However, it is important to consider the pressure sensitivity requirements when attemping to miniaturize, since the pressure sensitivity is also affected by the device dimensions. The sensitivity is a linear function of the diaphragm's stiffness, given by Equation 3.1. It is included here for convenience:

$$P = \frac{\pi^4 E H^3}{6(1-\nu^2)L^4} \cdot c$$

In order to maintain the current sensitivity, the ratio H^3/L^4 must be maintained. As the device scales down, H drops faster than L; the dimensions become more planar. This is ideal because the MEMS-based processing techniques used to fabricate the sensor all operate optimally on planar structures. Since PDMS microfabrication techniques are well-developed, the ability to scale the strain gauge dimensions will ultimately limit the miniaturization. The strain gauge thickness must scale linearly

with H to prevent it from stiffening one side of the diaphragm, and the features of the strain gauge pattern must also scale linearly with L.

With the current screen patterning technique used to create the strain gauge, it should be possible to reduce the thickness of the screen to ~ 25 μm before it becomes to fragile to withstand the scraping step.

4.8 Summary

This chapter describes experiments performed to characterize the dynamic response of the pressure sensor array. The results are used to develop and validate a model relating the differential pressure experienced by the diaphragm to the strain gauge's resistance change. The model breaks the pressure-resistance relationship into a large-amplitude component and a small-amplitude component. The small-amplitude component is linear, while the large-amplitude component is nonlinear but single-valued.

The operating conditions required for linear response are identified, and correspond to small-amplitude AC pressure signals, which are the main signals of interest in the lateral line application. This linear operating regime may be achieved by holding the underwater depth of the aquatic vehicle fixed. The tiny pressure signals generated by nearby objects are sufficiently small so that they mainly excite the small-amplitude response of the sensor. Table 4.3 lists the pressure sensitivities of each sensor, which are effectively the sensors' gains. For small-amplitude sensor output, obtaining the applied pressure involves a simple gain factor. For the large-amplitude DC sensor output, the corresponding applied pressure may be onbtained at the cost of additional signal processing due to the nonlinearity.

Finally, the voltage noise in the system is characterized and used to determine the pressure resolution of each sensor, given in Table 4.4. The sensors of the array have an average pressure resolution of 1.5 pascals, which exceeds the 10 pascal requirement of the lateral line application.

Chapter 5

Underwater Testing of the Pressure Sensor Array

The experiments documented in this chapter may be considered proof-of-concept demonstrations for the lateral line application, showing that the array is capable of operating underwater and transducing pressure signals as small as 10 pascals produced by relevent phenomena such as propogating waves and vortices. For these experiments, the array characterized in Chapter 4 is positioned below the surface of the water. The first experiment sends surface waves across the array, generating tiny cyclic, sinusoidal water pressure waves. The second experiment uses a foil dragged at an angle of attack to generate a vortex near the array. The output of the array is interpreted taking into account the behaviors described in Chapter 4.

5.1 Water-tank Experimental Setup

The underwater sensor experiments were conducted in a large 2.6 meter wide, 1.4 meter deep, 33 meter long water tank equipped with a surface wave generating machine. The large dimensions of the tank reduce the reflections of waves off the edges, reducing the interfering signals affecting the array's measurements.

The experimental setup, shown in Figure 5-1, is designed to test the pressure sensor array in conditions mimicking underwater deployment on the hull of an aquatic

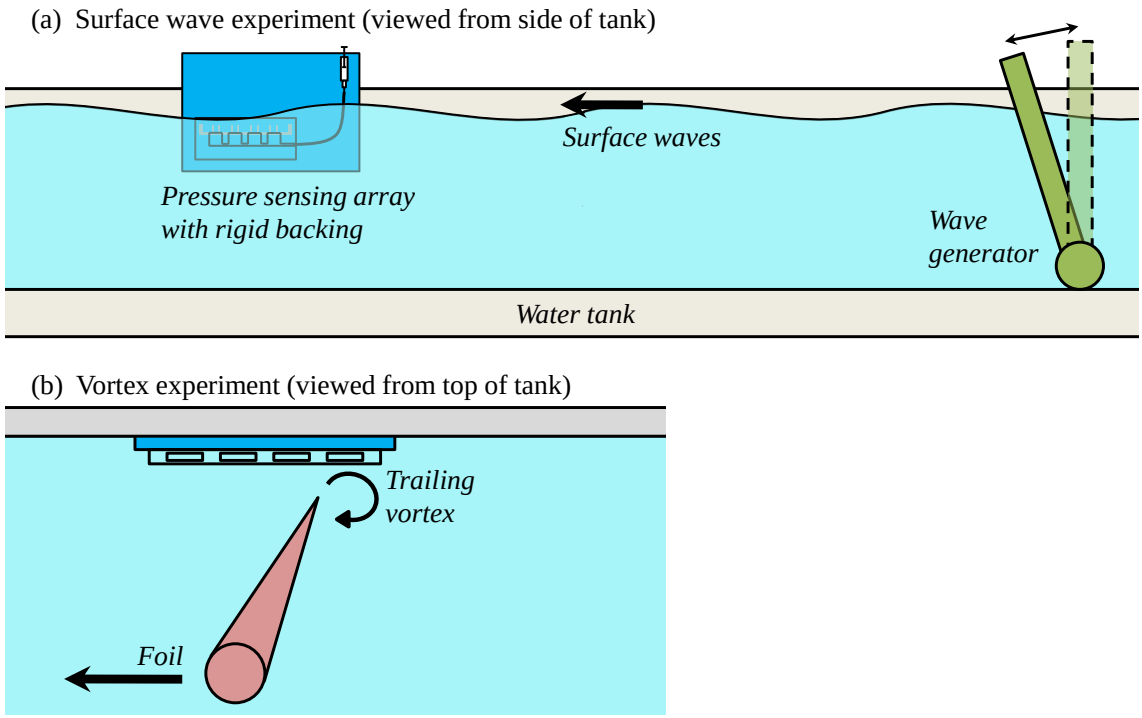

Figure 5-1: Diagram and picture of water tank experimental setups.

vehicle. In order to simulate the hull mount point, the array is mounted on a flat, rigid plate and submerged such that the diaphragm of each sensor is situated 3 cm below the water surface. The pressure equilibration channel is connected to a syringe which provides a positive bias pressure to the cavity. This causes the diaphragm to deflect outwards, allowing the strain gauges to operate in tensile strain as discussed in Section 4.4. The tube equilibration system described in Section 3.2.3 is not necessary since the array is mounted on a mockup hull that does not move. The syringe setup allows the cavity pressure to be changed more easily during testing.

It is important to note that the resistance data obtained from the sensor array is inverted compared to the pressure experienced by the sensors due to the pressure biasing scheme. External pressure acts to reduce the outward deflection of the diaphragm, reducing the strain on the strain gauge. Thus, higher external pressure corresponds to lower strain gauge resistance and a reduced output voltage in this biasing scheme.

The measurement circuit used in these experiments is identical to the setup described in Section 4.1.

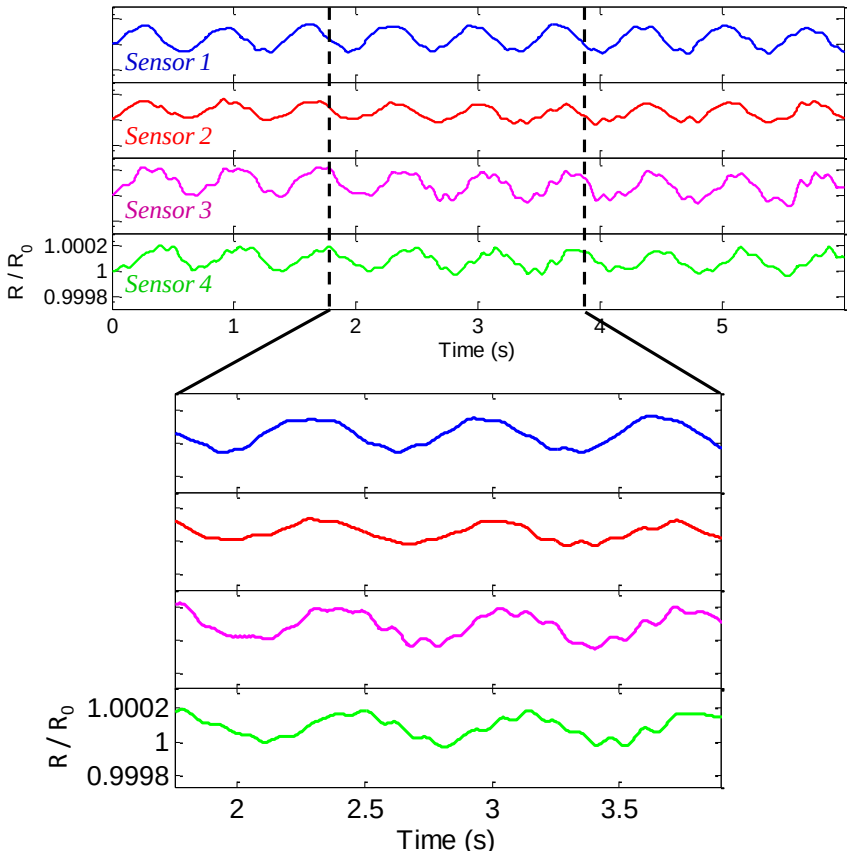

Figure 5-2: Pressure sensor array output in response to surface waves. The axis scaling is identical for all four plots. Greater resistance corresponds to lower pressure.

5.2 Detection of Surface Waves

As diagrammed in Figure 5-1(a), the wave machine is used to generate sinusoidal surface waves which propogate across the pressure sensor array. During the experiment, the center-to-peak amplitude A of the surface waves was measured to be 4 mm. Figure 5-2 plots a snapshot of the array output in response to the surface waves. The period of the surface waves is 0.67 s, determined using the time elapsed during 8 periods. This corresponds to a frequency f of 1.5 Hz. Based on the time offset $\Delta t = 0.2$ s between the waveforms of the Sensors 1 and 4, the velocity v of the waves is determined to be

$$v = \frac{D}{\Delta t} = \frac{45 \text{ mm}}{0.2 \text{ s}} = 22.5 \text{ cm/s} \tag{5.1}$$

where D is the spacing between the centers of Sensors 1 and 4. The wavelength λ may then be calculated as

$$\lambda = \frac{v}{f} = 15 \text{ cm} \tag{5.2}$$

Finally, the amplitude of the R/R_0 waveforms is coverted into a measured pressure. The Sensor 1 waveform in Figure 5-2 has an amplitude of 0.0001 fractional resistance change. From Table 4.3, the small-amplitude sensitivity G of Sensor 1 is given as a 0.0011 fractional resistance change per 100 pascals. Thus, the measured pressure amplitude P may be calculated as

$$P = \frac{1}{G} \cdot \frac{\Delta R}{R_0} = \frac{100 \text{ Pa}}{0.0011} \cdot 0.0001 = 9.1 \text{ Pa} \tag{5.3}$$

The pressure value obtained by Equation 5.3 may be compared with the pressure predicted by linear surface wave theory. This theory models the underwater pressure oscillations produced by the propogation of gravity waves over the surface of a fluid layer [19]. The pressure is composed of a static component P_s due to the average underwater depth of the array, and a dynamic component P_d due to the sinusoidal surface waves. P_d decays exponentially with water depth, since there is less flow farther away from the surface. The complete expression for the pressure P that the sensor array will experience is given by

$$P_{total} = P_s + P_d = \rho g y + \rho g e^{-ky} \cdot A cos(kx - \omega t) \tag{5.4}$$

where ρ is the density of water, g is the acceleration due to gravity, y is the depth of the sensors underwater, A is the amplitude of the surface waves, k is the wavenumber, and ω is the angular frequency. For this calculation, P_s will be ignored because it represents the operating depth of the sensor, to which the R/R_0 data is normalized. Thus, the amplitude of the pressure wave P reduces to

$$P = \rho g e^{-ky} \cdot A \tag{5.5}$$

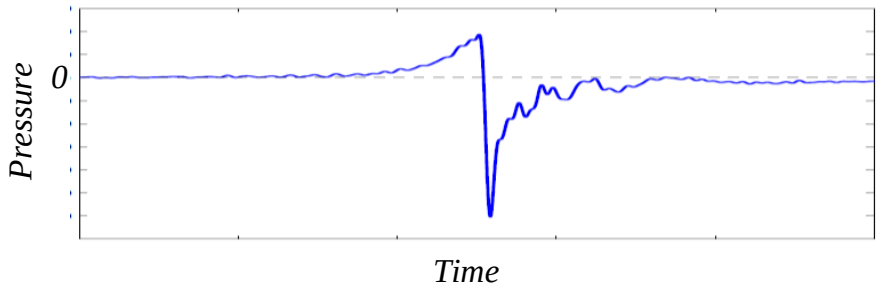

Figure 5-3: Figure courtesy of [7]. Typical underwater pressure trace generated by a rod with a square cross-section moving past a commercial pressure sensor.

Equation 5.5 evaluates to

$$P = 1000 \text{ kg/m}^3 \cdot 9.8 \text{ m/s}^2 \cdot exp(-\frac{2\pi}{0.15 \text{ m}} \cdot 0.03 \text{ m}) \cdot 0.004 \text{ m} = 11.2 \text{ Pa}$$

which is within 12% of the value measured by the pressure sensor array. The main source of error is likely measurement error of y, the depth of the array below the water surface. However, since y is a factor of 10 smaller than λ, the error should not exponentially affect the result.

Overall, the surface wave experiment demonstrates that the pressure sensor array is able to transduce a 10-pascal sinusoidal underwater pressure wave propogating sequentially across its sensors. Furthermore, this experiment demonstrates that it is possible to determine key parameters such as the wavelength and frequency of the propogating wave from the data produced by the array. Finally, the good numerical match between the predicted and measured pressure amplitudes demonstrates the sensor's quantitative accuracy.

5.3 Detection of a Vortex Induced by a Foil

For the lateral line application, it is important to test the array's response to an object moving across the sensors. Other works have provided pressure traces generated by a moving object. In [7], square and cylindrical rods are moved past discrete commercial pressure sensors in order to investigate how the shape of the rod affects the pressure trace. Figure 5-3 represents the typical form of a pressure trace produced by an object

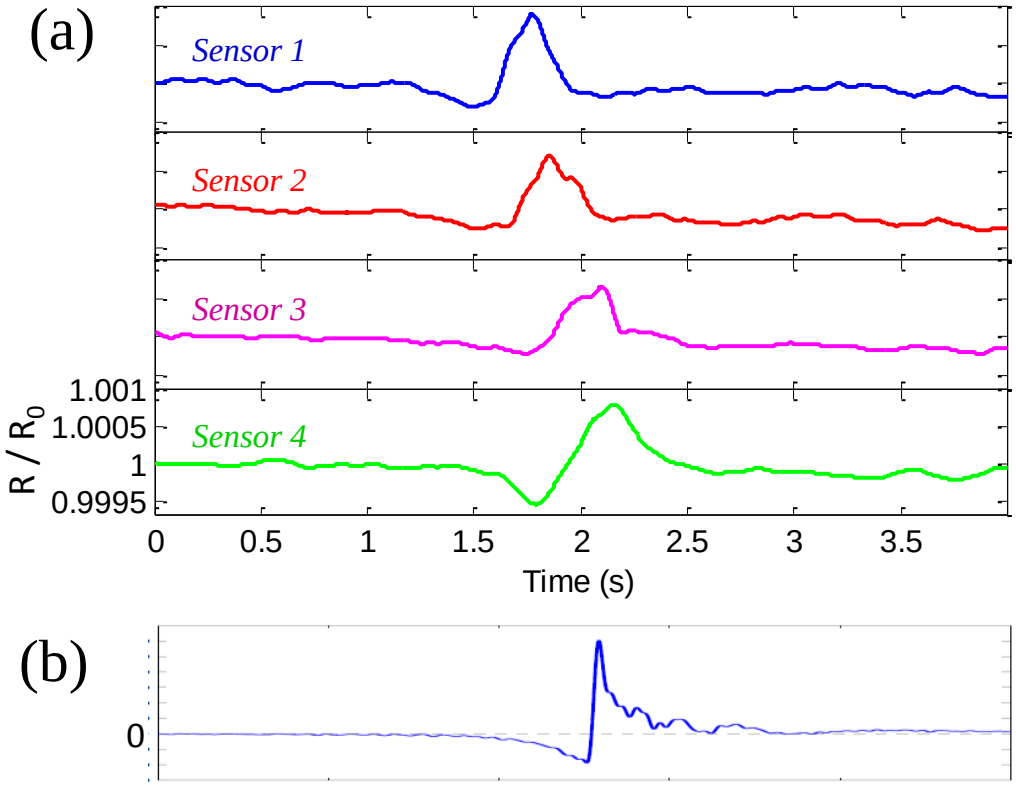

Figure 5-4: (a) Time-domain waveforms illustrating the output of the array's four sensors in response to a foil being dragged across the array. Greater resistance corresponds to lower pressure. (b) Figure 5-3 is reproduced here inverted and scaled for comparison with the measured data.

moving past a pressure sensor. The initial rise in pressure is created by the leading edge of the object, and the sudden drop in pressure corresponds to the moment the leading edge just passes the sensor. The gradual recovery of the pressure is caused by the presence of a vortex shed by the trailing edge of the object.

The goal of the experiment performed in this section is to see if the array is capable of producing the key features of the waveform shown in Figure 5-3 in response to a similar stimulus. Figure 5-1(b) diagrams this section's experimental setup. A foil is dragged across the pressure sensor array at a constant velocity with a high $\sim 70^o$ angle of attack. The foil passes the array with 2 cm of seperation. The array's response is plotted in Figure 5-4.

It is important to note that, just like in the surface wave experiments, a greater

resistance corresponds to a lower pressure due to the biasing scheme used. Thus, the initial dip in the R/R_0 waveform followed by a spike, and then a slower recovery back to neutral match well with the pressure waveform of Figure 5-3 and are precisely the features expected of this pressure waveform.

Using waveform analysis techniques that were presented in Section 5.2, the velocity v of the foil is calculated to be 12.2 cm/s. Using techniques described in [7], the data from the four traces may be used to interrogate the shape and distance to the object, though that analysis is not done here.

Chapter 6

Conclusions

This thesis develops a flexible elastomer-based underwater pressure sensor array from the ground up, beginning with the development of a carbon black-PDMS elastomer material set (Chapter 2). Using these materials, a 4-point-probe carbon black-PDMS resistive strain gauge is developed and combined with a pressure-concentrating PDMS diaphragm to create the MEMS-based pressure sensors (Chapter 3). The dynamic response of the sensors is characterized and modelled. Based on the model, the operating conditions required for a linear pressure-resistance response are determined (Chapter 4). This thesis ends with the proof-of-concept underwater object and wave detection experiments demonstrating that the sensor can function as an artificial lateral line (Chapter 5). When mounted onto an aquatic vehicle's hull, the array may provide obstacle detection, avoidance, and identification, underwater navigation, vortex tracking, and detection of flow separation.

The sensors exhibit a $1.38 \cdot 10^{-3}$ fractional resistance change per 100 pascals, with a coefficient of variation of 0.25 over the four sensors in the array (Table 4.3). This sensitivity yields a maximum pressure resolution of 1.5 pascals for a power consumption of 10 μW per sensor, ignoring the power dissipated by the amplification circuitry and parasitic series resistances (Table 4.4). Each sensor is capable of transducing up to a 1 kPa pressure signal across its 10 mm square diaphragm, though the sensor may respond to signals of this amplitude at arbitrary underwater depth due to the use of a pressure equilibration scheme. (Section 3.2.3). The overall array has a 15 mm

spatial resolution. An upper bound for the bandwidth of the diaphragms is calculated to be 940 Hz, ignoring viscous damping due to air, water, and the PDMS (Section 3.2.1). Additionally, sensor operation while mounted to a hull with a 0.5 m curvature is demonstrated (Section 3.2.4).

Compared to previous pressure sensing works using polymers and elastomers, this thesis provides a more thorough dynamic response characterization, accounting for the viscoleasticity of the PDMS and the nonlinear resistance-strain relationship of the carbon black-PDMS composite, while identifying an operating regime that maximizes the linearity of the sensor's response. The sensor array is designed to be easily fitted to the curved hull of an aquatic vehicle. Being made from relatively inert elastomers, the array is mechanical and chemically robust. Underwater experiments demonstrate the array transducing 10 pascal amplitude pressure signals produced by surface waves with quantative accuracy, as well as the characteristic pressure trace produced by a foil being dragged across the array. From the array output, the wavelength and frequency of the waves, and the velocity of the foil were able to be determined.

Overall, this MEMS-based elastomer pressure sensor array departs significantly from prior polymer and elastomer-based pressure sensors in that it is intended not for tactile applications, but for the lateral line application which requires high pressure sensitivity over a small range. This pressure sensor array is able to achieve the sensitivity requirements set by the lateral line application without requiring the cost and processing complexity of silicon, and is also able utilize the flexibility, chemical robustness, and waterproofing that the elastomer material set provides without becoming unusable due to hysteresis.

6.1 Summary of Research Contributions

This section briefly covers several important ideas, results, and discoveries that have come about from the development of the flexible underwater pressure sensor array. First, a carbon black-PDMS elastomer strain gauge technology is presented. Techniques for patterning the elastomer composite are developed. The strain gauge's dy-

namic response is characterized. The response is consistent with theories presented in literature stating that the carbon particles form conductive chains, and that changes in resistance result from breaking of these chains during strain.

The model developed and presented in this thesis extends the carbon-chain theory by postulating that very small strains should result in more reversible, linear resistance changes due to bending, rather than breaking, of the carbon chains. Based on this idea, model breaks the response into a large-amplitude component that is nonlinear but single-valued and monotonic, and a small-amplitude component that is linear. This idea is confirmed by comparing the experimental data with a numerical simulation which implements the model. Finally, using the model, operating conditions required for linear response are identified despite the inherent viscoelasticity of the elastomer materials. These conditions are met by small-amplitude AC signals. These results are promising and suggest that there are many applications for the carbon black-PDMS composite as a transduction element in applications where elastomer substrates are used.

The 4-point probe concept is used in the strain gauge for a myriad of reasons. It provides electrical isolation between sensors, while allowing them to operate off of the same current power supply. It increases sensitivity by solely measuring the resistance of the portion of the strain gauge located on the edge of the diaphragm where maximum strain occurs. Conversely, it desensitizes the sensor output to the contact resistance, parasitic series resistances, and mechanical coupling between sensors. It allows for the carbon black-PDMS composite to be used as a flexible wiring without reducing sensitivity due to series resistance. This relieves the brittle metal contacts from having to extend onto the active, straining region of the devices. All of these techniques which use the 4-point-probe concept may be useful for future elastomer-based electrical devices.

6.2 Future Directions

There are several research paths to follow from this point on. Some involve improve the performance and functionality of this pressure sensor array to the point where it may be used by existing AUVs. Others involve adapting the core technologies developed in the process of creating the array for other devices and applications. This section will peruse through a few of the more immediate, straightforward options, while the rest are left to the creativity of the reader.

Being based on MEMS technology, this device will have all the benefits that come with miniaturization - namely improved sensitivity, reduced power consumption, and higher bandwidth. However, significant miniaturization requires the existing fabrication technologies to be improved. Ideally, a photolithography-based patterning technique for the carbon black-PDMS composite would be developed. The dimensions of the device may also be optimized for sensitivity or packaging.

The material set also deserves a significant amount of attention. With the current carbon black-PDMS strain gauge, a scientific investigation into the resistance change mechanism could yield a quantative model derived from first principles, in contrast to the empirically derived model in this thesis. Knowledge of the mechanism could enable optimization of the material for increased sensitivity or linearity. Finally, only the tensile operating regime of the carbon black-PDMS strain gauge is investigated in this thesis. Further work characterizing the neutral strain and compressive strain regions should be done. In addition to carbon black, alternative conductive filler particles should be surveyed.

Outside of the realm of pressure sensors, the carbon black-PDMS material set could be used to create inexpensive large-area arrays of tactile, flow or temperature sensors for vehicles and robots alike. The author hopes that, based on the characterization and modeling presented in this work, these elastomers are able to open up a new application space not yet conquered by silicon devices.

Appendix A

Pressure-Resistance Simulation Script

Used in Section 4.3. Given time and pressure data as arguments `time` and `pref`, function `cb_nonlin2_sim` returns the simulated fractional resistance change as the variable `sim_frac_interp`, interpolated to correspond with `time`.

```
% ------------------------------------------------------------
%
% Frank Yaul 2011 June - Carbon black sensor simulation
% Input is pref vs. time, output x is fractional resistance change
%
% k,c,g1,g2 - Model parameters
% time,F - Experimental data
%
%
%        +--G--+
%    o---|     |---K--o
%        +--C--+
%
%    |----------|------|--> +Displacement, +External force
%               X1=0   X2=0
%
% (1) x1 = g1*Fg + g2*Fg^2
% (2) F = C*x1p + Fg
% (3) F = K*(x2-x1)
% Solve for x2p as a function of F, x2, and their derivatives
```

```
%
% ------------------------------------------------------------

function sim_frac_interp = cb_nonlin2_sim(time, pref)

% Material model parameters.
params = struct('G1', 10e-7, ...
    'G2', 1.2e-8, ...
    'C', 6e5, ...
    'K', 0.90e5 ...
    );

% ODE simulation
ode_func = @(t,x) cb_nonlin2_ode(t,x,time,pref,params);
[sim_time, sim_frac] = ode23(ode_func, [min(time) max(time)], [0]);
sim_frac_interp = 1 + interp1(sim_time, sim_frac, time, 'linear');
sim_frac_interp = sim_frac_interp + pref' / params.K; % Equation 3


% The ODE Function
function xprime = cb_nonlin2_ode(t,x,time,force,params)

G1 = params.G1;
G2 = params.G2;
C = params.C;
K = params.K;

% Get all of the data
x1 = x;
F = interp1(time, force, t, 'linear');

% Return
x1p = 1/C * (F - (sqrt(G1^2 + 4*G2*x1) - G1) / (2*G2)); % Equation 1 and 2

xprime = x1p;
```

References

[1] N. Andreadis et al. Fabrication of conductometric chemical sensors by photolithography of conductive polymer composites. *Microelec. Eng.*, 84:1211–1214, 2007.

[2] D. Bloor et al. A metal-polymer composite with unusual properties. *J. Phys. D: Appl. Phys*, 38:2851–2860, 2005.

[3] S. Coombs et al. Smart skins: Information processing by lateral line flow sensors. *Autonomous Robotics*, 11:255–261, 2001.

[4] T. Ding, L. Wang, and P. Wang. Changes in electrical resistance of carbon-black-filled silicone rubber composite during compression. *J. Poly. Sci. B: Poly. Phys.*, 45:2700–2706, 2007.

[5] W. P. Eaton and J. H. Smith. Micromachined pressure sensors: review and recent developments. *Smart Mater. Struct.*, 6:530–539, 1997.

[6] Z. Fan, J. Chen, D. Zou, J.and Bullen, C. Liu, and F. Delcomyn. Design and fabrication of artificial lateral line flow sensors. *J. Micromech. Microeng.*, 12:655–661, 2002.

[7] V. Fernandez, A. Maertens, F. M. Yaul, J. Dahl, J. H. Lang, and M. S. Triantafyllou. Lateral-line-inspired sensor arrays for navigation and object identification. *J. Marine Tech. Soc.*, 45(4), 2011.

[8] William Nichols Findley, James S. Lai, and Kasif Onaran. *Creep and Relaxation of Nonlinear Viscoelastic Materials*. Dover Publications, 1989.

[9] C. Gau, H. S. Ko, and H. T. Chen. Piezoresistive characteristics of a mwnt nanocomposite and fabrication as a polymer pressure sensor. *Nanotechnology*, 20, 2009.

[10] M. A. Gibbs. Lateral line receptors: Where do they come from developmentally and where is our research going? *Brain, Behavior, and Evolution*, 64:163–181, 2004.

[11] Honeywell International Inc. *19 mm Series Low Cost, Stainless Steel, Isolated Pressure Sensors*, 2008.

[12] D. W. Lee and Young-Soo Choi. A novel pressure sensor with a pdms diaphragm. *J. Microelec. Eng.*, 85:1054–1058, 2008.

[13] C. X. Liu and J. W. Choi. An ultra-sensitive nanocomposite pressure sensor patterned in a pdms diaphragm. *Proc. IEEE Transducers*, pages 2594–2597, 2011.

[14] V. Maheshwari and R. Saraf. Tactile devices to sense touch on par with a human finger. *Angew. Chem. Int. Ed.*, 47:7808–7826, 2008.

[15] J. C. McDonald et al. Fabrication of microfluidic systems in polydimethylsiloxane. *Electrophoresis*, 21:27–40, 2000.

[16] J.C. Montgomery, S. Coombs, and C.F. Baker. The mechanosensory lateral line system of the hypogean form of *Astyanax fasciatus*. *Environ. Biol. Fishes*, 62(1-3):87–96, 2001.

[17] Alan V. Oppenheim and Alan S. Willsky. *Signals & Systems*. Prentice Hall, 1997.

[18] K. Pohlmann, J. Atema, and T. Breithaupt. The importance of the lateral line in nocturnal predation of piscivorous catfish. *J. Exp. Biol.*, 207(17):2971–2978, 2004.

[19] R. H. Sabersky, A. J. Acosta, E. G Hauptmann, and E. M. Gates. *Fluid Flow*. Prentice Hall, 1998.

[20] F. Schneider et al. Mechanical properties of silicones for mems. *J. Micromech. and Microeng.*, 18, 2008.

[21] Stephen D. Senturia. *Microsystem Design*. Kluwer Academic Publishers, 2001.

[22] T. Someya et al. A large-area, flexible pressure sensor matrix with organic field-effect transistors for artificial skin applications. *Proc. Nat'l Acad. Sci.*, 101(27):9966–9970, 2004.

[23] C. Stampfer et al. Fabrication of single-walled carbon-nanotube-based pressure sensors. *Nano Letters*, 6(2):233–237, 2006.

[24] M. S. Triantafyllou and G. S Triantafyllou. An efficient swimming machine. *Scientific American*, 272(3):64–70, 1995.

[25] D. Vogel and H. Bleckmann. Behavorial discrimination of water motions caused by moving objects. *J. Comp. Physiol. A*, 186(12):1107–1117, 2000.

[26] C. von Campenhausen, I. Riess, and R. Weissert. Detection of stationary objects by the blind cave fish *Anoptichthys jordani* (characidae). *J. of Comp. Physiol. A Sens. Neural. Behav. Physiol.*, 143(3):369–374, 1981.

[27] L. Wang, T. Ding, and P. Wang. Thin flexible pressure sensor array based on carbon black/silicone rubber nanocomposite. *IEEE Sensors*, 9(9):1130–1136, 2009.

[28] Y. Yang, J. Chen, C. Tucker, S. Pandya, D. Jones, and C. Liu. Biomimetic flow sensing using artificial lateral lines. *ASME Conf. Proc*, 43025:1331–1338, 2007.

[29] Y. Yang et al. Distant touch hydrodynamic imaging with an artificial lateral line. *Proc. Nat. Acad. Sci.*, 103(50):18891–18895, 2006.

[30] D. Young. Vibration of rectangular plates by the ritz method. *J. Appl. Mech*, 17:448–453, 1950.

[31] J. Yuh. Design and control of autonomous underwater robots: A survey. *Autonomous Robots*, 8:7–24, 2000.